AlGaAs Microring Resonators For All-Optical Signal Processing

Prova Christina Gomes

A thesis submitted to the Faculty of Graduate and Postdoctoral Studies in partial fulfillment of the requirements for the degree of

MASTER OF APPLIED SCIENCE

in Electrical and Computer Engineering

Supervised by
Professor Ksenia Dolgaleva

Ottawa-Carleton Institute for Electrical and Computer Engineering
University of Ottawa
September, 2016

Abstract

Photonic integration and all-optical signal processing are promising solutions to the increasing demand for high-bandwidth and high-speed communication systems. III-V semiconductor materials, specially AlGaAs, have shown potentials for photonic integration and efficient nonlinear processes due to their low nonlinear absorption, flexibility at controlling the refractive index, and mature fabrication technology.

In this thesis, we report the designs of AlGaAs microring resonators optimized for efficient four-wave mixing. Four-wave mixing (FWM) is a nonlinear optical phenomenon which can be used to realize many optical signal processing operations such as optical wavelength conversion and optical time division multiplexing and demultiplexing. Our designed AlGaAs microring resonators are expected to have good optical confinement, transmission characteristics, and efficient coupling between the ring and waveguide.

Here we also present our fabrication efforts to fabricate the microring resonators device and the insights gained in the process. The microring resonators devices have a potential to be used in optical communication networks for all-optical signal processing operations.

Acknowledgments

I would like to express my greatest appreciation and gratitude to my supervisor, Prof. Ksenia Dolgaleva for her support, guidance, and wise supervision. Her deep insights helped me at many stages of my research and my growth as a researcher. She is not only a great supervisor but also a great teacher. I feel very fortunate for having the opportunity to have her as my mentor.

I am thankful to the fellow graduate students and post-docs from Prof. Dolgaleva's research group. I am especially grateful to Kashif Awan for his guidance in this project and contribution towards the fabrication of the microring resonators device. Many thanks to Dr. Lilian Sirbu for his support with the simulations. I would also like to thank Dr. Mikko Huttunen, Payman Rasekh, Shayan Saeidi, and Saad Bin Alam.

I would like to acknowledge Zhongfa Liao and Pisek Kultavewuti from Professor Aitchison's group in the University of Toronto for the fabricating the device. I would also like to thank Cornell nanofabrication facility for letting us use their fabrication facility.

Finally, I would like to express my profound gratitude to my husband Tahmid, my mother Anna, my father John, and my brother Shuvo for their endless support and encouragement in every steps of my life. This accomplishment would not have been possible without them.

Statement of Originality

I declare that the work in this thesis has not previously been submitted for a degree or diploma at any university. I certify that the literature review, simulations, and the design parts of this thesis are the products of my own work. For fabrication, the credit for the two e-beams and the second etching process discussed in this thesis, the SEM images, and the optical micrographs goes to Zhongfa Liao from the University of Toronto. Also, the credit for first etching process and SEM images goes to Kashif Awan from the University of Ottawa.

Prova Christina Gomes

Table of Contents

1 Introduction **1**

1.1 Motivation 1

1.1.1 Why Microring Resonators? 3

1.1.2 Why Aluminium Gallium Arsenide (AlGaAs)? 4

1.2 Objectives 6

1.3 Outline of the Thesis 6

2 Theory of Microring Resonators **8**

2.1 Introduction to Waveguides 8

2.2 Principle of Operation of Microring Resonators 12

2.2.1 Coupling of Optical Power 13

2.2.2 Critical Coupling 17

2.3 Spectral Parameters 17

2.3.1 Free Spectral Range (FSR) 17

2.3.2 Full-Width at Half Maximum (FWHM) 19

2.3.3 Finesse 19

2.3.4 Quality factor 20

2.4 Types of Microring Resonators 21

2.4.1 All-pass resonators 21

2.4.2 Add-Drop Resonators 23

2.4.3 Racetrack Microring Resonators 25

2.4.4 The Lateral and Vertical Coupling Configuration 26

2.4.5 Cascaded Microring Resonators 28

3 Nonlinear Effects and All-Optical Signal Processing 31

3.1 Nonlinear Optical Effects 31

3.1.1 Four-Wave Mixing 32

3.1.2 Self-Phase Modulation 33

3.1.3 Cross-Phase Modulation 35

3.2 All-Optical Signal Processing 36

3.2.1 All-Optical Wavelength Conversion 36

3.2.2 Optical Time Division Multiplexing and Demultiplexing . . . 38

4 Design of Microring Resonators and Numerical Results 40

4.1 Material Composition 40

4.2 Design Criteria for Microring Resonators 42

4.3 Design and Results 44

4.3.1 Modal Analysis 46

4.3.2 Dispersion Analysis 50

4.3.3 Transmission Analysis 51

4.3.4 FSR and Q-factor 57

4.3.5 Four-Wave Mixing Simulation 59

4.4 Tapers 61

5 Fabrication of AlGaAs Microring Resonators 63

5.1 Fabrication Process 63

5.2 Fabrication of Microring Resonators 66

6 Summary 73

Bibliography 75

List of Figures

2.1 The basic structure of waveguide showing the core and cladding layers. 8

2.2 Reflection and refraction of light at the interface between two media with different refractive indices. 9

2.3 Propagation of light inside a waveguide governed by total internal reflection. 10

2.4 Examples of different types of 2D waveguides: (a) Rib Waveguide, (b) Strip-loaded Waveguide, (c) Nanowire, and (d) Optical Fiber. 11

2.5 Schematic diagram showing a four-port integrated optical microring resonator. 12

2.6 The schematic of Racetrack Microring Resonator showing the coupling length. 14

2.7 Schematic diagram illustrating the coupling between a ring and a straight waveguide. The figure is reproduced after Yariv [51]. 14

2.8 A typical transmission spectrum showing Free Spectral Range (FSR) and Full Width at Half Maximum (FWHM). 19

2.9 Transmission spectrum at through port of an all-pass resonator. . . . 22

2.10 Effective Phase shift as a function of the single-pass phase shift of an all-pass resonator with nearly zero intrinsic losses ($a \approx 1$), plotted for different values of t. 23

2.11 Add-drop microring resonator. 24

2.12 Transmission spectrum at through and drop port of add-drop resonator. 25
2.13 Schematic diagram of Racetrack Microring Resonator. 26
2.14 Microring resonator coupling arrangements: (a) lateral coupling, (b) vertical coupling. 27
2.15 Cross section of the lateral coupling. 28
2.16 Cross section of the vertical coupling. 28
2.17 Schematics of higher order microring resonators with (a) serial and (b) parallel configuration. 30

3.1 Schematic of the four-wave mixing effect in an optical $\chi^{(3)}$ medium. . 32
3.2 Schematic diagram of (a) degenerate and (b) non-degenerate FWM in the frequency. domain 33
3.3 Schematic of self-phase modulation (SPM) and cross-phase modulation (XPM). 34
3.4 Wavelength converter based on nonlinear wave-mixing effect. 37
3.5 Four-wave mixing between the information channels and two non-modulated pulse streams resulting in the multiplexing of the three channels into a higher-bit-rate stream. 39

4.1 AlGaAs Wafer composition. 41
4.2 Schematic of the waveguide dimensions. 45
4.3 Tapered AlGaAs microring resonator. 45
4.4 Simulation layout of the waveguide. 47
4.5 Intensity distribution of fundamental (a) TE mode and (b) TM mode of a straight AlGaAs waveguide of width 0.4 μm. 48
4.6 Effective refractive index (n_{eff}) of the fundamental TE and TM mode as a function of wavelength. 49
4.7 Intensity distribution of the fundamental TE mode in the coupling region. 49

4.8 The dispersion characteristics of the fundamental TE and TM modes of an AlGaAs waveguide. The waveguide has the width 0.4 μm, the core ($Al_{0.18}Ga_{0.82}As$) thickness 0.6 μm, the upper cladding ($Al_{0.65}Ga_{0.35}As$) thickness 0.4 μm. The total thickness of lower cladding is 3 μm where the etch depth goes 0.4 μm into the lower cladding. 51

4.9 The layout of the microring resonator simulation in Lumerical MODE solutions. 52

4.10 The schematic of the add-drop microring resonator with the parameter ranges specified on the drawing. 53

4.11 Transmission spectrum at the through port of an all-pass ring resonator. The radii of the half rings are 8 μm, coupling length and the gap between straight waveguide and coupling waveguide are 3 μm and 0.1 μm, respectively. The widths of all the waveguides are 0.4 μm. . . 54

4.12 Finite difference time domain (2.5D FDTD) simulation demonstrating the optical power build-up at 1.5567 μm in a microring resonator. The ring radius is 4 μm, the coupling length is 5 μm and the gap between the straight waveguide and coupling region of the ring is 0.1 μm. The widths of both straight waveguide and ring are 0.4 μm. 55

4.13 Transmission spectra of the through and drop ports of an add-drop ring resonator. Here, the radii of the half rings are 5 μm, the coupling length and the gap between the straight and coupling waveguides are 3 μm and 0.1 μm, respectively. The widths of all the waveguides are 0.4 μm. 55

4.14 The value of the normalized transmitted power at the through and drop ports at the resonant wavelength around 1.55 μm of a microring resonator as a function of the gap width between the straight waveguide and the ring. The ring resonator has a racetrack structure. The radii of the half rings are 8 μm, and length of coupling region is 7 μm. . . . 57
4.15 Calculated FSR (in nm) as a function of the round trip length (in μm) of an AlGaAs microring resonator at the wavelength 1.55 μm . Here, the radius and coupling length vary with the round-trip length, and the width of the waveguides is set to 0.4 μm. 58
4.16 Calculated Q-factor as a function of the round trip length (μm) of AlGaAs microring resonators. Here, the propagation loss of the waveguide is set to 5.7 dB/mm. 60
4.17 The schematic of the four-wave mixing in an all-pass microring resonator. 60
4.18 Simulation result showing generation of idler at 1.521 μm by a 1.554 μm pump and 1.588 μm signal. 61
4.19 The top view of the structure and dimension of the spot-size converter used to taper down the input beam into the straight waveguide of our designed microring resonator. 62

5.1 Steps of the fabrication process. 65
5.2 SEM image showing a microring resonator after the development. . . 68
5.3 A fragment of the sample containing microring resonators photographed under the optical microscope. 69
5.4 SEM images of two waveguides which are (a) 80 nm, (b) 100 nm, and (c) 120 nm apart. (d) SEM image of a straight waveguide with the width 2 μm. 70

5.5 SEM images showing the etched (a) cross-section of the waveguide, and (b) a 200 nm gap between the ring and straight waveguide. 72

List of Tables

1.1 The promises and challenges of all-optical signal processing and photonic integration. 2

4.1 The coupled power to the ring and power at the drop port for different radii of the half rings, coupling lengths, and gap widths between the straight waveguide and ring. The resonant wavelength around 1.55 μm was selected. Here, the width of all the waveguides is 0.4 μm, as other widths resulted in worse transmission characteristics. 56

Chapter 1

Introduction

1.1 Motivation

In the 21st century, the communication industry is witnessing a major demand for data bandwidth as the popularity of high-speed multimedia services and Internet is increasing exponentially. According to CISCO, only the monthly global mobile data traffic will surpass 24.3 exabytes by 2019 [1]. The conventional ways of signal processing using electronics or optoelectronics are facing difficulties keeping up with this increasing demand and almost hitting the fundamental limits. To solve this issue, new devices and technologies with higher bandwidths are needed, and a promising solution for future high-speed communication systems is all-optical signal processing.

Over the past decade, many all-optical signal processing functions like optical wavelength conversion [2,3], multiplexing-demultiplexing [4,5], channel extraction [6], regeneration [5, 7, 8], switching [9] have been explored. All-optical signal processing could potentially occur at a much higher speed compared to electronic signal processing due to the much higher bandwidth associated with optics. In addition, all-optical signal processing does not require the optical to electrical to optical (OEO) signal conversion if the signals are already in the optical domain. Also, unlike the electronic

devices, optical devices do not need to switch every bit of the signal bit stream in order to process it. For example, optical amplifiers can amplify Tb/s signals without switching in bit level. However, unlike electronics, optics has shortage in the area of information storage or memory. In addition, the high costs of assembling of discrete optics represent a major obstacle. A solution to this problem is the integration of optical devices, which enables a substantial progress in the realization of more cost-effective solutions to achieve a high-speed connectivity.

Photonic integrated circuit (PIC) integrates multiple optical components in a small chip. PICs have already shown promises for applications such as, optical wavelength division multiplexing-demultiplexing, quantum computing, optical interconnects, optical networks, lab-on-chip, *etc.* Reduced size, lower cost, higher functionalities, and, most importantly, efficient coupling between passive waveguides and active III-V semiconductor devices are the main advantages of PIC. However, the progression of PIC is still slow because of the complexity of the material system compared to the electronics. Table 1.1 summarizes the promises and challenges of all optical signal processing and photonic integration.

Promises	Challenges
Large Bandwidth	Lack of optical memory
Ultra fast speed	Expensive
Small footprint	Complex material system
Lower energy consumption	Lack of digital processing system
Lower heat dissipation	

Table 1.1: The promises and challenges of all-optical signal processing and photonic integration.

In this Master of Applied Science work, we have been attempting to contribute

towards the development of integrated photonic circuits to enable all-optical signal processing devices. More specifically, we focused on the design and realization of the microring resonators based on aluminium gallium arsenide (AlGaAs) III-V semiconductors as it shows potentials for photonic integration and all-optical signal processing. The next two sections explains the motivation behind choosing microring resonators and the material AlGaAs for our research.

1.1.1 Why Microring Resonators?

In order to meet the current demand for efficient communication, the all-optical signal processing system must be able to demonstrate faster speed, lower fabrication cost, compact footprint, and integration capability. Also, the implementation of all-optical networks requires a collection of passive and active devices, *e.g.* wavelength converters, filters, couplers, multiplexers, demultiplexers, and optical amplifiers.

The idea of optical ring resonators first came out in late 1960s [10]. It is a device which consists of rings and straight waveguides, and exhibits a discrete set of frequency resonances. The radius of the ring of a ring resonator can be anywhere between several meters (*e.g.*, optical fibres) [11] to micrometers (*e.g.*, integrated optical devices) [12, 13]. The microring resonator with a radius of a few micrometers is an ideal candidate for all-optical signal processing applications because of its narrow bandwidth with a wide free spectral range (FSR).

The microring resonators have already proven to be ideal candidates for integrated high-quality optical signal processing devices. Nonlinear optical processes in microring resonators can be utilized to achieve all-optical signal processing. To ensure efficient nonlinear optical interactions at the expense of the lower loss, the material composition needs to be selected in such a way that, the energy of the photons that interact with the material is below half the band-gap energy of the material. The ability

of microring resonators to resonate the radiation with the wavelengths matching its resonances to extend the interaction length makes the optical nonlinearity to appear stronger. Extending the length of the nonlinear interactions requires taking care of phase matching. This is where sub-micrometer waveguides come in handy: because of the dispersion management they offer through their strong waveguide dispersion.

Besides, the possibility of frequency comb generation by cascaded four-wave mixing using microring resonators [14–16] is an extremely important feature in novel integrated photonic circuits. Because of the compact size of microring resonators and low operating power, the frequency comb generation based on microresonators show great potential in applications ranging from on-chip frequency references [17] to high-speed telecommunications [18].

The micrometer order size of the microring offers the advantage of integrating thousands of devices in a small chip. Moreover, the fabrication of microring resonators is straightforward compared to other types of resonators as there is no need for any mirrors, bragg gratings, or distributed feedback waveguides to achieve the positive feedback.

In the communication sector, various all-optical applications have been demonstarted using microring resonators, such as filters [13, 19], wavelength converters [20], channel extraction [21], multiplexing-demultiplexing [22, 23]. Apart from communication systems, microring resonators are also used in other scientific and medical sector, *e.g.*, biosensing [24–26], ultrasound detection [27], humidity sensor [28], eye surgery [29].

1.1.2 Why Aluminium Gallium Arsenide (AlGaAs)?

Over the past several years, silicon has received a lot of attention for its potentials in optical integration. The availability of well developed relatively simple growth proce-

dure that relies on Czochralski pulling method makes silicon inexpensive and readily available in large volumes. Numerous studies and consecutive commercialization attempts have helped to establish a low-cost well developed fabrication technology for silicon photonic circuits. The unique capability offered by silicon is the monolithic integration of optical and electrical devices. However, silicon is an indirect band-gap semiconductor, which makes it next to impossible to produce electrically pumped light sources based on this material. To produce a silicon-based photonic chip, one has to resort to hybrid integration with other materials such as III-V semiconductors in order to implement the light sources. Despite the fact that the value of the Kerr coefficient of silicon is relatively high ($n_2 = (4.5 \pm 1.5) \times 10^{-18}$ m^{2}W^{-1} at 1.55 μm [30]), it cannot be thought of as a suitable candidate for all-optical signal processing operations because it exhibits significant nonlinear losses in the telecom wavelength range (1400 nm to 1600 nm) due to two-photon absorption and the absorption by the induced free-carriers [31–33].

Suitable characteristics of materials for communications include low linear and nonlinear material absorption, mature fabrication technology, control over the refractive index, monolithic integration, and suitable nonlinear optical properties. Many ternary and quaternary III-V semiconductors, such as, AlGaAs [34,35], InGaAsP [36], InGaP [37], InAsP [38, 39], InGaN [40–42], AlGaAsP [43] have already been investigated for their optical responses. Among all these materials, AlGaAs stands out as a promising candidates for all-optical signal processing. It has been termed "the silicon of nonlinear optics" [44] due to its excellent nonlinear optical performance [44–48] that entails the combination of a very high value of the Kerr coefficient with the negligible nonlinear absorption. It has the highest Kerr nonlinearity ($n_2 = 1.43 \times 10^{-17}$ m^{2}W^{-1} for TM polarization [46]) compared to other candidates suitable for all-optical signal processing. The high refractive index of AlGaAs in the range of 3.3 at the telecom wavelength allows for a tight mode confinement for more efficient nonlinear interac-

tions. By changing the aluminum concentration of $Al_xGa_{1-x}As$ from $x = 0$ to $x = 1$ during the growth process, one can adjust the refractive index of the material in the range between 3.38 and 2.90 in the telecom C-band. This property offers flexibility in designing different AlGaAs integrated components.

AlGaAs is a direct bandgap material which allows monolithic integration of both active and passive devices on the same chip. Also, the nonlinear optical interactions in AlGaAs are not limited to the third-order nonlinear effects. The magnitude of the nonlinear refractive coefficient of AlGaAs is around 500 times that of silica. As AlGaAs is a noncentrosymmetric material, it also exhibits second-order nonlinearities with the value of $\chi^{(2)}$ around 200 pmV [49]. In addition, recent advances in AlGaAs fabrication have enabled the fabrication of ultracompact low-loss waveguides capable of competing with silicon waveguides [50]. Due to all these reasons, AlGaAs is an ideal candidate to realize all-optical signal processing devices on-a-chip in general, and our research goals in particular.

1.2 Objectives

The goal of this Masters thesis research is the design and realization of AlGaAs microring resonators optimized for efficient four-wave mixing at the telecommunication wavelength range.

1.3 Outline of the Thesis

Chapter 1 of this thesis describes the motivation of our research and gives an overview of the semiconductor materials and the microring resonators in the context of all-optical signal processing. Chapter 2 reviews the theory, the principle of operation, the parameters dictating the performance and different types of microring resonators.

The fundamentals of nonlinear optical effects and all-optical signal processing are discussed in Chapter 3. We introduced the nonlinear optical phenomena crucial for all-optical signal processing. Among those are four-wave mixing, self-phase modulation, and cross-phase modulation. We also give some examples of simple optical signal processing operations, such as all-optical wavelength conversion and optical time division multiplexing demultiplexing, which rely on the discussed nonlinear effects. In Chapter 4, we present the design and simulation results for the microring resonators. In Chapter 5, we discuss our attempted fabrication procedures for the microring resonators and the valuable information they gave us that could be implemented in future fabrication development. Finally, Chapter 6 summarizes the accomplishments of this dissertation.

Chapter 2

Theory of Microring Resonators

2.1 Introduction to Waveguides

An optical waveguide is a structure which guides electromagnetic waves of the optical spectrum in accordance with the principle of constructive interference and total internal reflection. The general structure of a dielectric optical waveguide (see Fig. 2.1) consists of a core and claddings. The core is a high-refractive-index optical medium which is surrounded by low-refractive-index cladding.

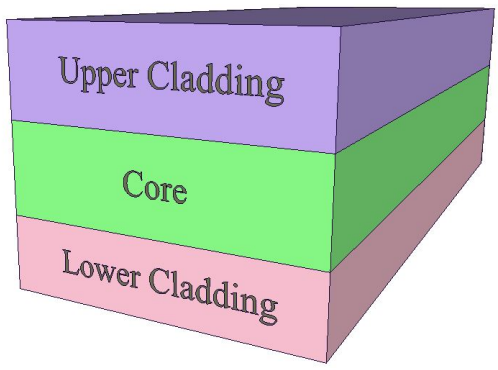

Figure 2.1: The basic structure of waveguide showing the core and cladding layers.

The propagation of light through such structure can be understood in terms of the ray optics model that relies on the Snell's Law. The Snell's Law governs the reflection

and refraction at the boundaries between two media with different refractive indices (see Fig. 2.2). According to Snell's second law:

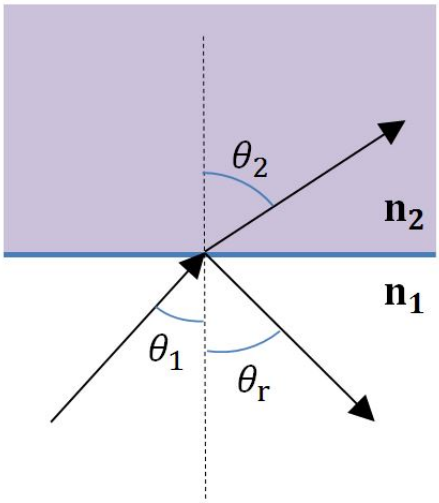

Figure 2.2: Reflection and refraction of light at the interface between two media with different refractive indices.

$$n_1 \sin\theta_1 = n_2 \sin\theta_2. \tag{2.1}$$

Here n_1 and n_2 are the refractive indices of medium 1 and medium 2, respectively. The angle of incidence is θ_1 and the angle of refraction or transmission is θ_2, which are measured with respect to the normal at the boundary. Let us assume now that $n_1 > n_2$. When the angle of incidence θ_1 is relatively large, such that, the light can no longer penetrate to the medium 2, the total internal reflection (TIR) occurs. When the refracted light lies along the boundary, having an angle of refraction of 90°, the angle of incidence is called the *critical angle* (θ_c). For the angle of incidence greater than the critical angle, all the incident light reflects from the boundary and total internal reflection occurs. To be guided inside a waveguide the incident light should satisfy the condition for the total internal reflection and the angle of incidence of the light rays propagating from the core towards the interface with the claddings should

be

$$\theta_1 > \theta_c = \sin^{-1}\left(\frac{n_2}{n_1}\right). \tag{2.2}$$

For the angle of incidence greater than the critical angle, the total internal refection occurs, and the light propagates inside a waveguide at an angle θ_r. Fig. 2.3 shows a schematic of such propagation where the refractive index of the core is n_1 and the refractive index of the claddings is n_2.

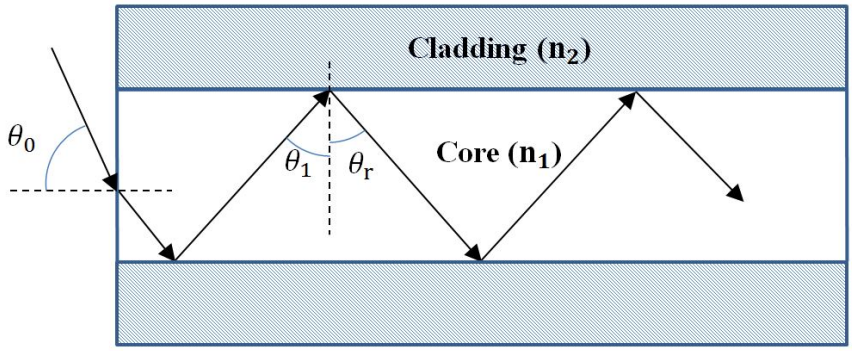

Figure 2.3: Propagation of light inside a waveguide governed by total internal reflection.

There is another angle associated with the propagation of light through waveguides, known as the *acceptance angle* (θ_0). The acceptance angle is the maximum allowable angle of the incident ray coming into the waveguide structure from outside with respect to the optical axis of the waveguide. The acceptance angle of a waveguide can be written as:

$$\theta_0 = \sin^{-1}\left(\frac{\sqrt{n_1^2 - n_2^2}}{n_0}\right). \tag{2.3}$$

Here n_1, n_2, and n_0 are the refractive indices of the waveguide core, cladding, and surrounding media, respectively.

The waveguides can be classified based on their geometries. The waveguides with

1D confinement (where the core and claddings represent infinite slabs) are typically called slab dielectric waveguides. The slab waveguides can, in turn, be classified into symmetric and asymmetric, depending on whether the claddings to the two sides of the core are of the same or of different kind. The waveguides with 2D confinement can occur in a variety of geometries. Some of them are depicted in Fig. 2.4.

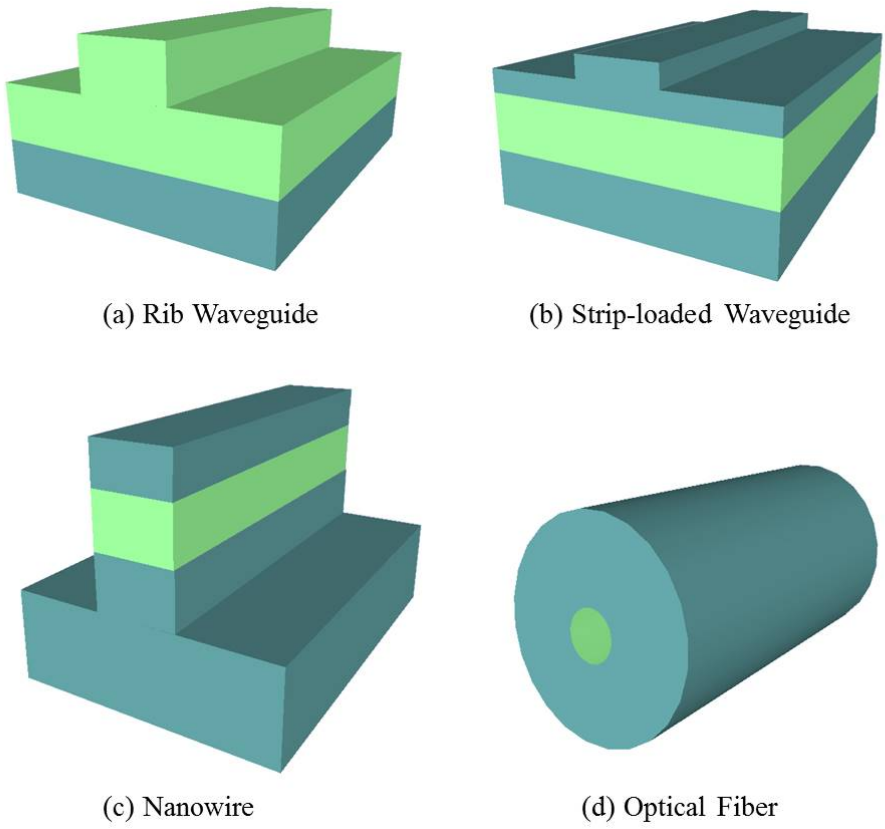

Figure 2.4: Examples of different types of 2D waveguides: (a) Rib Waveguide, (b) Strip-loaded Waveguide, (c) Nanowire, and (d) Optical Fiber.

Optical waveguides are the building block of any integrated optical components. That is why, it is important to start any design from the design of the waveguide cross-sections. For the present thesis work, we'll be focusing on the nanowire geometry as this type of waveguide is appropriate for the microring resonators.

2.2 Principle of Operation of Microring Resonators

A ring resonator is a device that exhibits a discrete set of frequency resonances. This device consists of rings and straight waveguides. In Fig. 2.5, we show the schematic of an integrated optical ring resonator with four ports. Such a configuration is called an *add-drop filter*. Light passing through the input port can get coupled into the ring, provided that its frequency coincides with one of the resonant frequencies of the ring. The four ports of an add-drop filter are known as input port, through port, drop port and add port. The input port is used to provide light source to the device. Some of the input light gets coupled to the ring and comes out of the drop port. Coupling between the straight waveguides and ring is achieved through the evanescent waves. The light that was not coupled to the ring comes out from the through port. Add port is used if any additional signal needs to be added to the device.

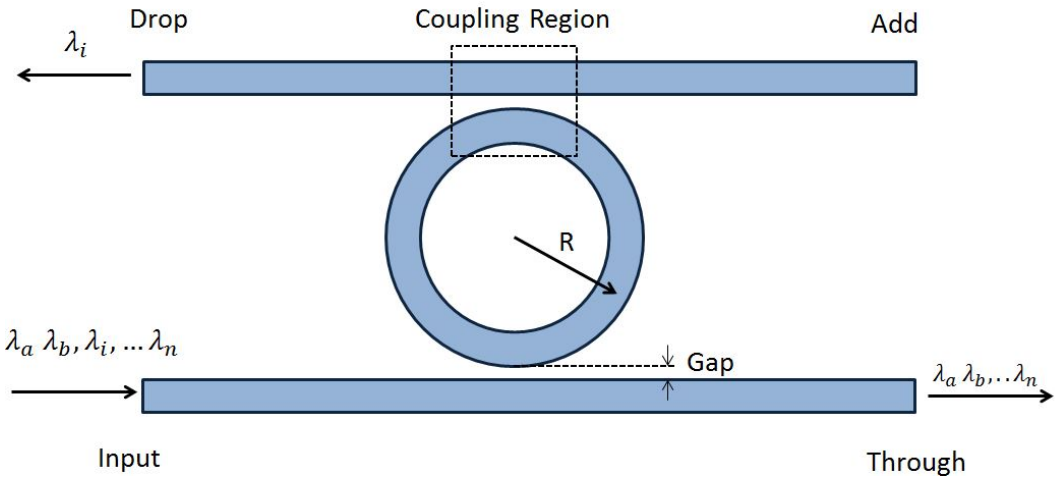

Figure 2.5: Schematic diagram showing a four-port integrated optical microring resonator.

The spectrum of a microring resonator can be characterized by a set of discrete resonances with the wavelengths satisfying the following resonant condition:

$$n_{\text{eff}} L = m\lambda_i. \tag{2.4}$$

Here, λ_i is the input wavelength, n_{eff} is the effective refractive index of the waveguide mode, L is the optical path length of the ring ($2\pi R$), and m is an integer ($m = 1, 2, 3, \cdots$) which represents the number of resonance. Ring resonators can support multiple resonances. Assume that the light propagating through the input port of a microring resonator consists of multiple spectral components λ_a, λ_b, *etc.* (see Fig. 2.4). The spectral components satisfying the resonant condition (2.4) can be dropped from the original spectrum via getting coupled into the ring, and later into the drop port waveguide (*e.g.*, λ_i in Fig. 2.4).

The gap between the ring and the straight waveguides, the length of the region where the waveguide and the ring are evanescently coupled (coupling length), and the refractive index difference between the ring and the straight waveguide are important factors determining how much optical power can be coupled between the ring and the straight waveguide. The smaller the gap between the ring and straight waveguide in coupling region, the stronger the coupling. For a given coupling efficiency, the gap can be enlarged if the coupling length is increased. Coupling length can be increased by using a *racetrack configuration* [Fig. 2.6] of ring resonator. In the racetrack structure, instead of a full ring, there are two half-rings connected by two straight waveguides. This allows the device to have greater a coupling region. The refractive index of the guiding layer in the straight waveguide and ring resonator must be greater than the refractive index of the surrounding media in order to ensure the light confinement in the core of the device.

2.2.1 Coupling of Optical Power

When the ring and the waveguides are close enough (the gap is relatively small), the optical power transfer between them takes place. In order to better understand how does the coupling between the ring and waveguide occurs, let us consider a diagram

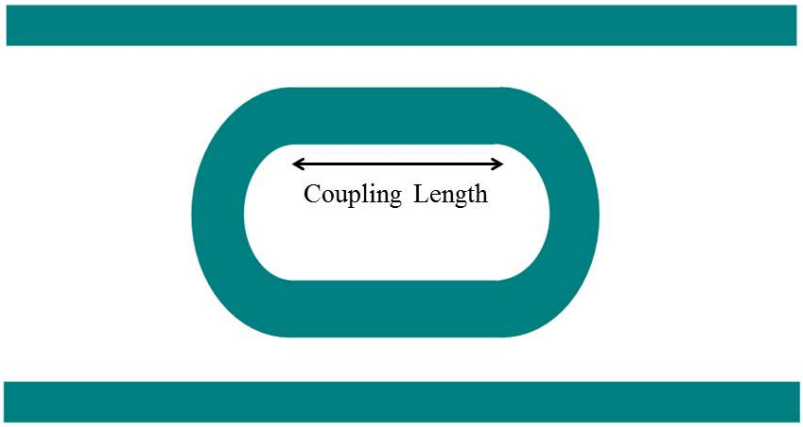

Figure 2.6: The schematic of Racetrack Microring Resonator showing the coupling length.

[Fig. 2.7] similar to that from the paper by Yariv [51].

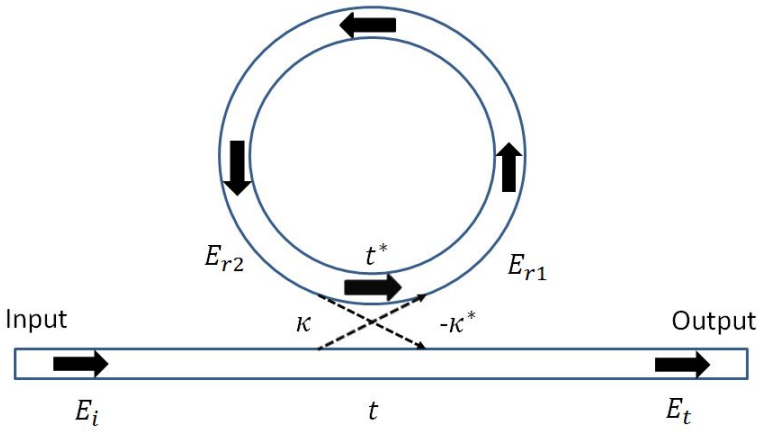

Figure 2.7: Schematic diagram illustrating the coupling between a ring and a straight waveguide. The figure is reproduced after Yariv [51].

Provided that the coupling is lossless, *i.e.*, the propagation losses in the waveguide and ring at the scale of the coupling length can be neglected, and there is no scattering and back-reflection, the interaction in the coupling region can be described by the

matrix relationship:

$$\begin{bmatrix} E_t \\ \\ E_{r1} \end{bmatrix} = \begin{bmatrix} t & \kappa \\ \\ -\kappa^* & t^* \end{bmatrix} \begin{bmatrix} E_i \\ \\ E_{r2} \end{bmatrix}. \tag{2.5}$$

Here, t is the self-coupling coefficient and κ is the cross-coupling coefficient. The self-coupling coefficient (t), specifies the fraction of the amplitude transmitted on each pass of light through the coupler, and the cross-coupling coefficient (κ) specifies the fraction of the amplitude is coupled to the ring. Also, E_i is the complex mode amplitude of the input field and E_t is the complex mode amplitude of the output field at the through port. All complex mode amplitudes E are normalized so that their squared magnitude corresponds to the modal power (*e.g.* , $|E_{\mathrm{t}}|^2 = P_{\mathrm{t}}$). For complete lossless coupling the relation below must be satisfied:

$$|\kappa|^2 + |t|^2 = 1. \tag{2.6}$$

To make all field amplitudes normalized to the input, the amplitude of E_i is taken to be as 1. The field propagating in the ring can be written as

$$E_{r2} = ae^{i\theta}E_{r1}, \tag{2.7}$$

where a is the the single-pass amplitude transmission, including both propagation loss in the ring and loss in the couplers. It relates to the power attenuation coefficient (α) as $a = exp(-\alpha L/2)$. θ is phase shift per round trip inside the ring. For a passive resonator, $a < 1$ and for zero internal loss $a = 1$. If optical amplification is available in the region of the ring, $a > 1$ can be achieved [52]. Using Eqs. (2.5) through (2.7), we can write the following expressions for the electric field amplitudes:

$$E_t = \frac{-a + te^{-i\theta}}{-at^* + e^{-i\theta}}, \tag{2.8}$$

$$E_{r2} = \frac{-a\kappa^*}{-at^* + e^{-i\theta}}, \tag{2.9}$$

$$E_{r1} = \frac{-\kappa^*}{1 - at^* e^{i\theta}}. \tag{2.10}$$

Using Eqs. (2.8) through (2.10), we can write the transmission power at the output of the waveguide and the total circulating power:

$$P_t = |E_t|^2 = \frac{a^2 + |t|^2 - 2a|t|cos(\theta + \phi_t)}{1 + a^2|t|^2 - 2a|t|cos(\theta + \phi_t)}; \tag{2.11}$$

$$P_{r2} = |E_{r2}|^2 = \frac{a^2(1 - |t|^2)}{1 + a^2|t|^2 - 2a|t|cos(\theta + \phi_t)}. \tag{2.12}$$

Here, $t = |t|cos(j\phi_t)$, $|t|$ represents the coupling loss, ϕ is the single pass phase shift of the coupler, $\phi = \beta L$, where β is the propagation constant and L is the round-trip length or the circumference of the ring. The resonant condition of this type of ring resonator is $\theta + \phi_t = 2\pi m$, where m is an integer.

The magnitude of the ratio of the field circulating inside the resonator E_{r2} to the input field E_i at the resonance ($\phi = 0$) is defined as the *enhancement factor* (EF):

$$EF = \left| \frac{E_{r2}}{E_i} \right| = \frac{\kappa}{1 - at}. \tag{2.13}$$

The higher the EF, the higher the intensity build up inside the ring resonator, and thus the lower is the amount of the input power required to induce nonlinear optical effects.

2.2.2 Critical Coupling

Let us now take a derivative of Eq. (2.13) with respect to the coupling coefficient κ, and set the result equal to zero. This would allow us to obtain the condition for the maximum achievable EF: the condition of *critical coupling*. We find that the critical coupling condition can be met when $a = |t|$. Under this condition, the resonant optical field gets entirely coupled into the ring, and no light comes out through the output port. Which means all the power coupled to the resonator is equal to the power lost inside the resonator. By this way, the ratio of the transmitted power to the incident power could be controlled through the adjustment of either a or t. In high-quality ring resonators (with the Q-factors on the order of 1000s or larger), even the smallest changes in the parameters a and t could result in large variations of the transmission characteristics. Another approach of controlling the critical coupling as well as the Q-factor of the resonator is by altering the internal loss in the ring using an integrated semiconductor optical amplifier [53]. Critical coupling is used in the application of wavelength selective switching and modulation [52].

2.3 Spectral Parameters

In this section, we describe some spectral parameters that characterize the performance of a microring resonator. Important parameters for microring resonators are free spectral range (FSR), full width at half maximum (FWHM), finesse, and quality factor.

2.3.1 Free Spectral Range (FSR)

Free Spectral Range (FSR) is the wavelength difference between two consecutive resonances in the transmission spectrum of the microring resonator (see Fig. 2.8). At

resonance, $\omega T_R = m2\pi$, where T_R is the round-trip time and m is an integer. Then, the two successive resonances, ω_1 and ω_2, are related as [54]:

$$FSR_{\text{frequency}} = \omega_2 - \omega_2 = \frac{2\pi}{T_R} = \frac{2\pi c}{Ln_{\text{eff}}}. \tag{2.14}$$

Translating the frequency term of FSR into wavelength, we get

$$FSR_{\text{wavelength}} = \frac{\lambda^2}{Ln_{\text{eff}}}. \tag{2.15}$$

Here, L is the optical path length of the ring ($L = 2\pi R$) and n_{eff} is the effective refractive index of the waveguide.

If the wavelength dependence of the effective index can not be neglected, the group refractive index (n_g) can be used instead of the effective index (n_{eff}) whenever appropriate. The modified FSR is then given by

$$FSR_{\text{wavelength}} = \frac{\lambda^2}{Ln_{\text{g}}}. \tag{2.16}$$

here n_{g} is defined as:

$$n_{\text{g}} = n_{eff} - \lambda\frac{\partial n_{eff}}{\partial \lambda}. \tag{2.17}$$

It can be seen from Eq. 2.16 that FSR is inversely proportional to the size (L) of the ring resonator. Some applications may require a relatively large value of FSR (on the order of a few nm). In order to achieve larger values of FSR, one should design a ring resonator with a relatively small footprint.

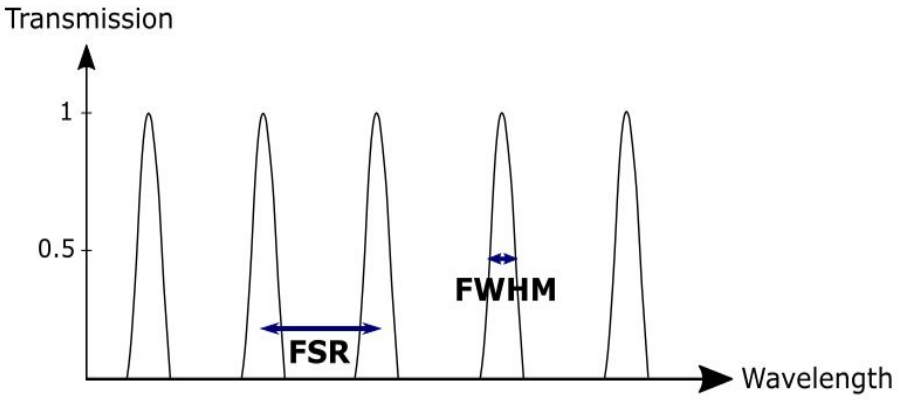

Figure 2.8: A typical transmission spectrum showing Free Spectral Range (FSR) and Full Width at Half Maximum (FWHM).

2.3.2 Full-Width at Half Maximum (FWHM)

The term full-width at half-maximum (FWHM) is used to define the bandwidth of a curve where the function reaches half of its maximum value. In a transmission spectrum, the FWHM is the wavelength range where the signal is attenuated to its 3-dB level (or to 1/2 of its maximum value). Fig. 2.8 shows FWHM of a resonance peak in a transmission spectrum. Assuming the self-coupling coefficient $t_1 = t_2 = t$ for add-drop resonator, we can express the FWHM of a microring resonator as:

$$FWHM = \frac{\lambda^2}{\pi L n_g} \frac{1 - at}{\sqrt{at}}. \tag{2.18}$$

2.3.3 Finesse

Finesse is the ratio between the FSR and the Full Width at Half Maximum (FWHM) of the resonator. Its value depends on the number of round trips that the energy can travel in the resonator before getting lost due to some associated loss mechanisms. The higher the finesse - the better is the resonator (the lower are the internal losses associated with the device). For an ideal lossless resonator, the value of the finesse tends to infinity: $\mathscr{F} \to \infty$. Using Eqs. (2.15) and (2.18) the finesse of a lossy

resonator:

$$\mathscr{F} = \frac{FSR}{FWHM} = \left(\frac{\lambda^2}{Ln_{\mathrm{g}}}\right)\left(\frac{\pi Ln_{\mathrm{g}}}{\lambda^2}\frac{\sqrt{at}}{1-at}\right) = \pi\frac{\sqrt{at}}{1-at}. \tag{2.19}$$

In the case where internal loss is negligible and coupling to the bus waveguides is symmetric and weak ($\kappa << 1$),

$$\mathscr{F} \approx \frac{\pi}{\kappa^2}. \tag{2.20}$$

2.3.4 Quality factor

Quality factor (Q-factor) measures the sharpness of the resonance relative to the central frequency. The Q-factor is usually defined as the ratio of the stored energy circulating inside the resonator to the energy lost per optical cycle:

$$Q = \omega_o \frac{\text{Stored energy}}{\text{Power loss}}. \tag{2.21}$$

The Q-factor of a microring resonator is defined as the ratio of the operation wavelength and the resonance FWHM:

$$Q = \frac{\lambda_{\mathrm{res}}}{FWHM} = \frac{\pi Ln_{\mathrm{g}}}{\lambda}\frac{\sqrt{at}}{1-at}. \tag{2.22}$$

The Q-factor represents the number of oscillations of the field before the circulating energy is attenuated down to 1/e with respect to its initial value. The round trip losses, as well as coupling losses acquired in the directional couplers, are the loss factors that need to be reduced in order to obtain high-Q resonances [55].

Implementing Eqs. (2.19) and (2.22), we can arrive at the relationship between the quality factor and the finesse:

$$Q = \frac{n_g L}{\lambda} \mathscr{F}. \tag{2.23}$$

2.4 Types of Microring Resonators

The building blocks of the microring resonators consist of a microring cavity and straight waveguides. Moreover, depending on the configuration and the number of straight waveguides, one can discriminate between different kinds of microring resonators. Also, it is not always necessary for a microring resonator to have a circular shape. Any geometrical path will act like a ring if it is closed.

2.4.1 All-pass resonators

The simplest form a ring resonator is an all-pass resonator (see Fig. 2.7). Such a device is comprised of a ring and a single straight waveguide. All-pass resonators delay signals by storing the incoming optical energy temporarily within the ring. Eqs. (2.11) and (2.12) give the transmission power at the output and total circulating power of an all-pass resonator. The wavelengths which coincide with the resonances gets coupled into the ring, and the rest of the wavelengths pass through the bus waveguide. Figure 2.9 shows the transmission spectrum of an all-pass resonator with the ring radius 16 μm, $a = 0.9$, and $t = 0.75$. One can see a sharp drop of the intensity at the through port at the resonant wavelengths.

The phase of the transmitted light is not always the same for different frequencies of light, especially those near resonances. The effective phase shift is defined as the phase argument of the field transmission factor. For the situations where the resonator losses could be neglected ($a \approx 1$), an effective phase shift of light going from input port to the through port of an all pass ring resonator can be written as [56]

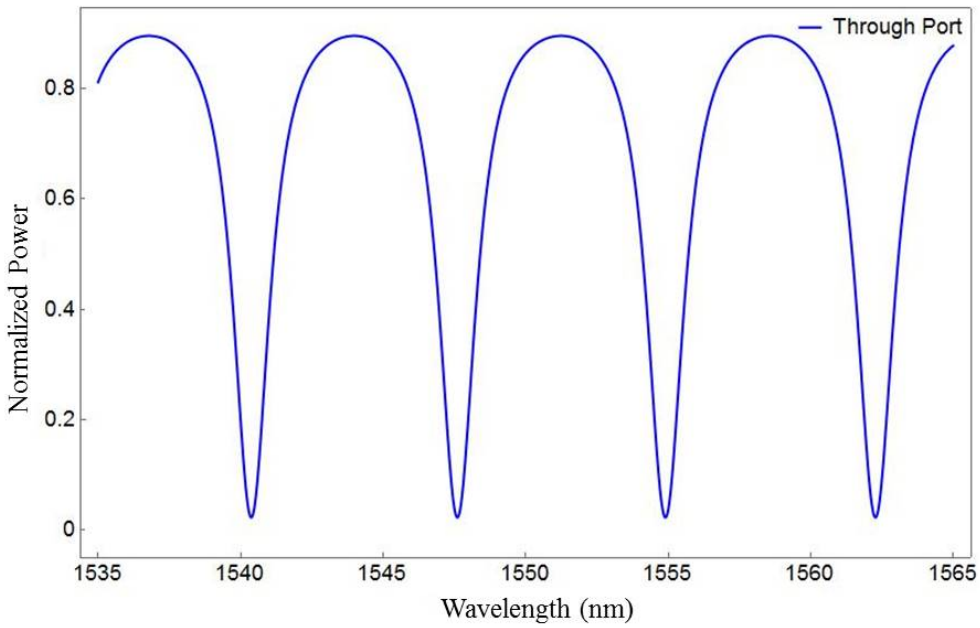

Figure 2.9: Transmission spectrum at through port of an all-pass resonator.

$$\varphi = \pi + \phi + 2\arctan\frac{t\sin\phi}{1 - t\cos\phi}. \tag{2.24}$$

Fig. 2.10 shows the plot of the effective phase shift as a function of a single-pass phase shift for an all-pass resonator for different values of t. The slope of the curves becomes very steep near the resonance ($\phi = 0$), which indicates that the overall output phase of the resonator becomes very sensitive to the small variations in the single-pass phase. This phase shift can be measured if we place a microring resonator near one arm of a Mach-Zender interferometer (MZI). It is a key parameter in designing notch filters based on microring resonators [57].

Round trip losses and coupling losses are important aspects to determine the Q-factor. Lower losses will lead to higher Q-factor. Therefore while operating close to the critical coupling an all-pass resonator shows higher Q-factor than an add-drop resonator [55].

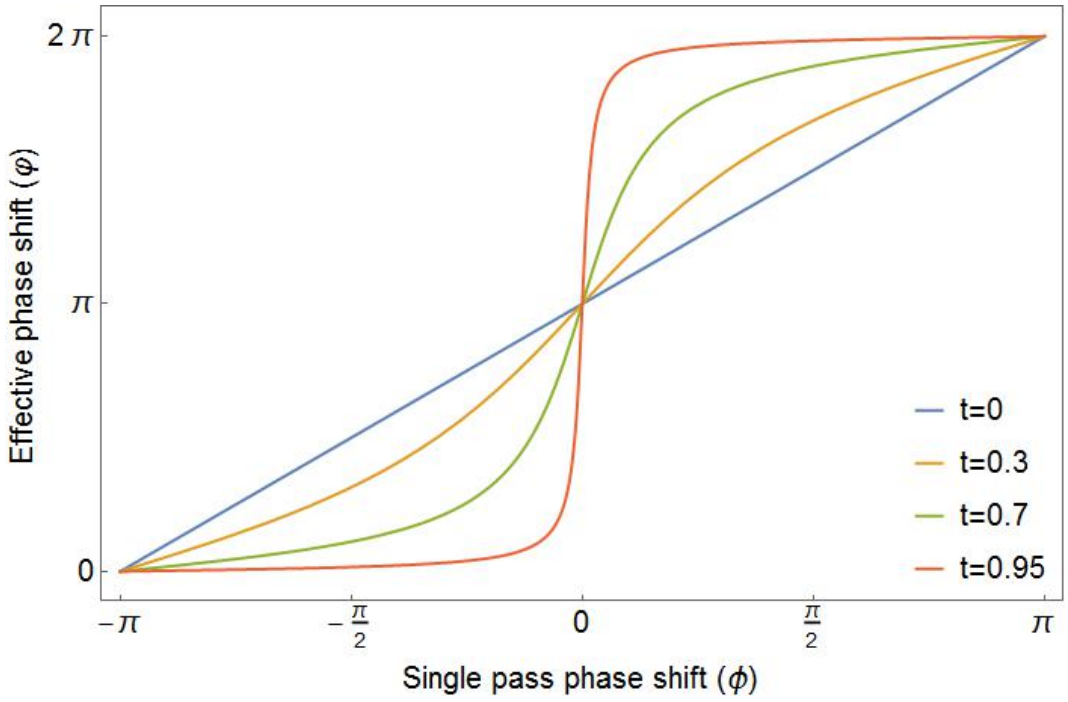

Figure 2.10: Effective Phase shift as a function of the single-pass phase shift of an all-pass resonator with nearly zero intrinsic losses ($a \approx 1$), plotted for different values of t.

2.4.2 Add-Drop Resonators

The schematic diagram of an add-drop microring resonator is represented in Fig. 2.11. This configuration contains a ring and two straight waveguides. Here the light with the wavelengths coinciding with the resonances of the ring comes out from the "drop" port.

Under the steady-state condition, the field amplitudes at the drop and through ports are given by the equations

$$E_{\text{drop}} = \frac{-\kappa_1^* \kappa_2 a_{1/2} e^{j\theta_{1/2}}}{1 - t_1^* t_2^* a e^{j\theta}} \tag{2.25}$$

and

$$E_{\text{through}} = \frac{t_1 - t_2^* a e^{j\theta}}{1 - t_1^* t_2^* a e^{j\theta}}. \tag{2.26}$$

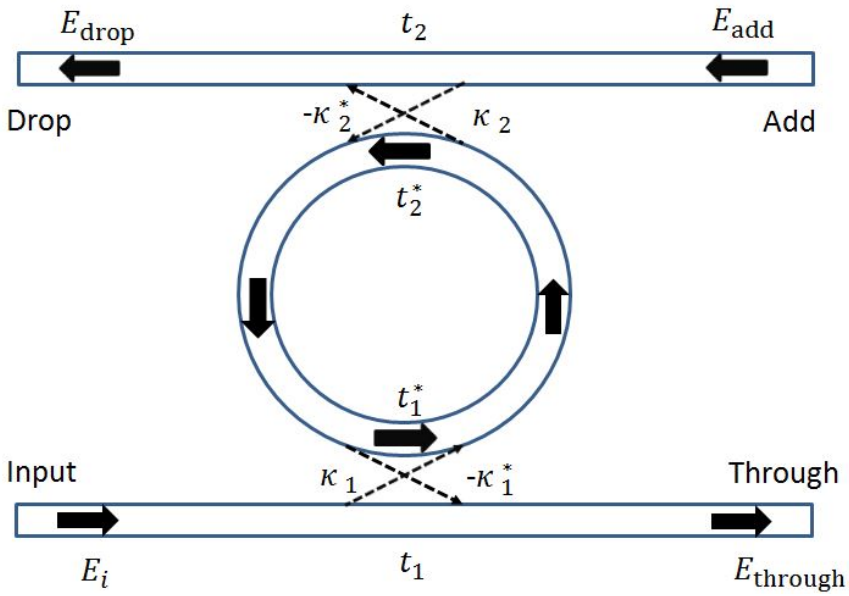

Figure 2.11: Add-drop microring resonator.

Here, t_1 and t_2 are the self-coupling coefficients of the input-through waveguide and add-drop waveguide respectively, which specify the fraction of the input amplitude transmitted on each pass of light through the coupler. κ_1, κ_2 are the the cross-coupling coefficients which specify the fraction of the input amplitude is being coupled from the input-through waveguide to the ring and from the ring to the add-drop waveguide respectively. In this analysis, $a_{1/2}$ and $\theta_{1/2}$ are used which are the loss and phase shift per half round trip inside the ring. Fig. 2.12 shows the intensity spectrum at the drop and through ports of a ring resonator with the radius 9 μm, $a = 0.98$, and $t_1 = t_2 = 0.85$.

The output power at the drop port at the resonance is given by the equation

$$P_{\text{drop}} = |E_{\text{drop}}|^2 = \frac{(1-|t_1|^2).(1-|t_2|^2)a}{(1-a|t_1 t_2|)^2}. \tag{2.27}$$

The add-drop resonators can be used as filters [58], sensors [59], multiplexers [60], *etc.*

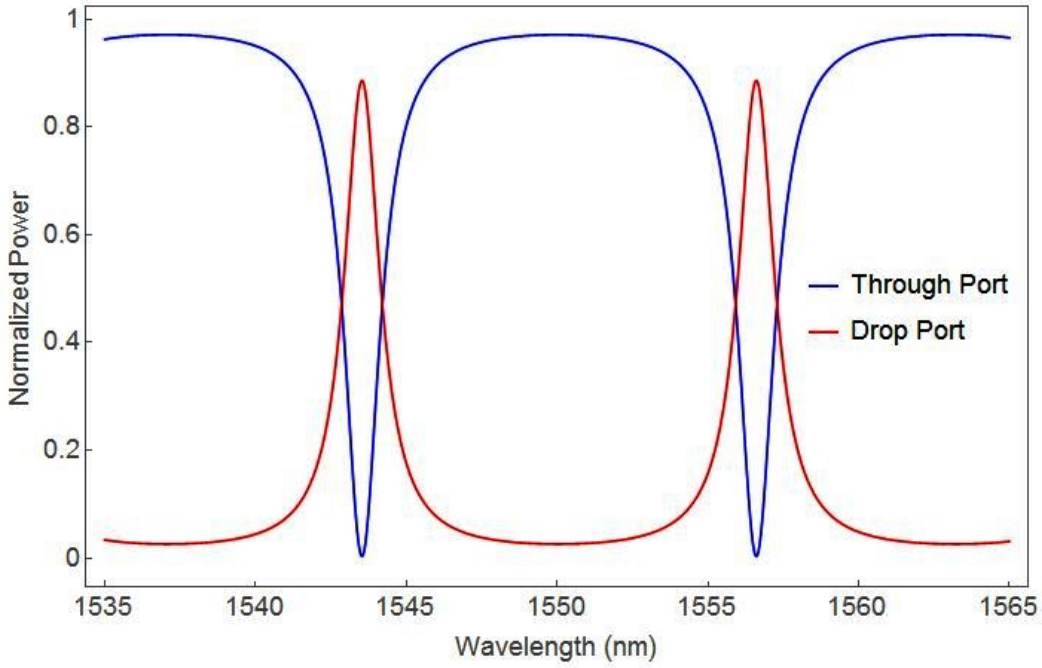

Figure 2.12: Transmission spectrum at through and drop port of add-drop resonator.

2.4.3 Racetrack Microring Resonators

As discussed earlier in Section 2.1, the coupling efficiency of a microring resonator can be enhanced by increasing the coupling length of the ring. One such configuration with the increased coupling length is called *racetrack microring resonator*. In this configuration the coupling region is extended by placing two straight waveguides in the middle of the ring (see Fig. 2.13). These extensions increase the coupling efficiency, with some reduction in the FSR. There are minor additional losses, called *junction losses*, associated with the extended coupling regions.

At the transitioning region between the straight and the curved waveguides, the propagation mode will change adiabatically between the normal mode in the straight waveguide and the radial mode in the curved waveguide.

For racetrack microring resonators, it is important to consider the change of phase difference ϕ at the coupling region in both couplers between self-coupling coefficient

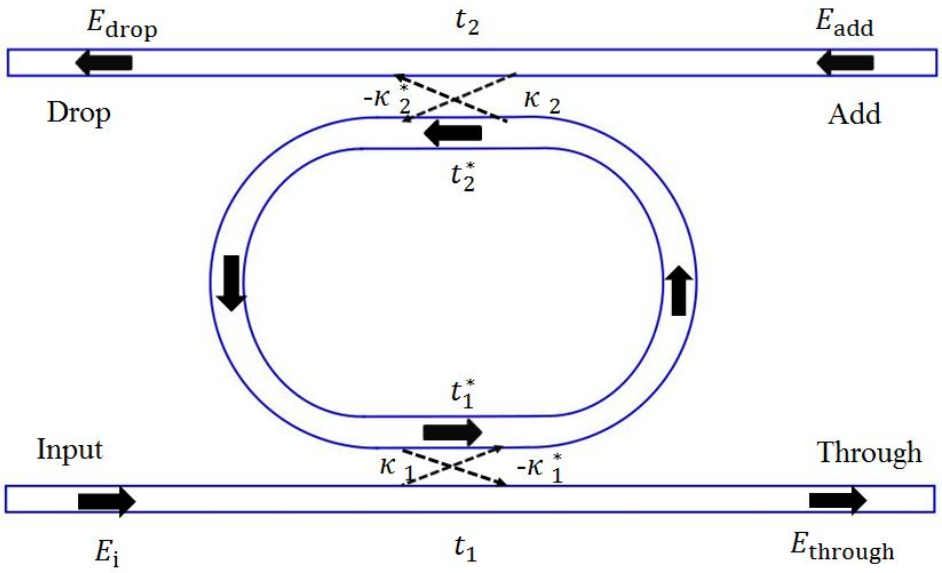

Figure 2.13: Schematic diagram of Racetrack Microring Resonator.

(t) and cross-coupling coefficient (κ). The phase difference depends on the length of the straight waveguide section and affects the output characteristics, as well as the resonant condition. In steady state, this phase difference can be used in Eqs. (2.25) and (2.26) using the method described in Lee et al. (2004) to describe the field amplitude at the through and drop ports of racetrack microring resonator:

$$E_{\mathrm{t}} = \frac{t_1 e^{j\phi_{t1}} - t_2^* a_{1/2}^2 e^{j\theta}(t_1 t_1^* e^{j2\phi_{t1}} - \kappa_1 \kappa_1^* e^{-j2\phi_{\kappa 2}}) e^{j\phi_{t2}}}{1 - t_1^* t_2^* a_{1/2}^2 e^{j\theta} e^{j\phi_{t1}} e^{j\phi_{t2}}} \tag{2.28}$$

and

$$E_{\mathrm{d}} = \frac{-\kappa_1^* \kappa_2 a_{1/2} e^{j\theta_{1/2}} e^{-j\phi_{\kappa 1}} e^{-j\phi_{\kappa 2}}}{1 - t_1^* t_2^* a e^{j\theta} e^{j\phi_{t1}} e^{j\phi_{t2}}}. \tag{2.29}$$

The resonant condition of racetrack microring resonator is $(\theta + \phi_{t1} + \phi_{t2}) = 2\pi m$.

2.4.4 The Lateral and Vertical Coupling Configuration

The coupling in a microring resonator could be achieved using one of two different arrangements: lateral and vertical coupling.

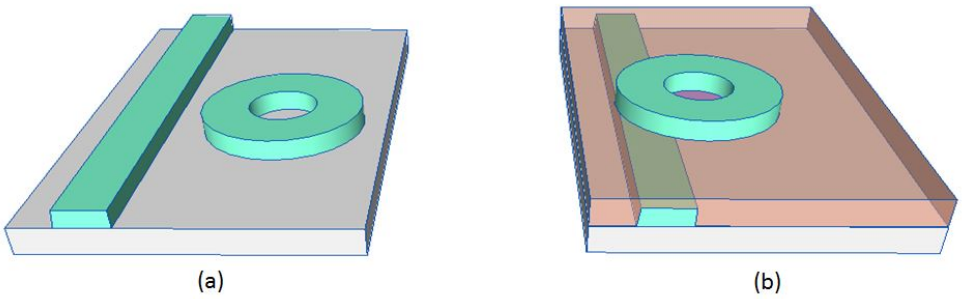

Figure 2.14: Microring resonator coupling arrangements: (a) lateral coupling, (b) vertical coupling.

In the lateral coupling configuration [see Figs. 2.14 (a) and 2.15] the ring and the input-output straight waveguides lie in the same plane. In this arrangement, the optical coupling occurs horizontally. In such a way, the coupling efficiency can be controlled through adjusting the horizontal gap between the ring and the straight waveguides. A microring resonator with lateral coupling requires a high-precision lithography and etching to achieve the desired gap between the ring and straight waveguides. The desired gap dimension depends largely on the material of choice and the refractive index contrast of the waveguides. For the high-index-contrast waveguides, the gaps with the dimensions on the order of tens to a hundred nanometers could be required. In that case high-resolution e-beam lithography is necessary to construct the gap. Also, in lateral coupling, since both the ring and the straight waveguides are fabricated in the same plane, they cannot be optimized individually.

Another coupling configuration, named *vertical coupling*, involves placing the ring and the straight waveguides in different layers [see Figs. 2.14 (b) and 2.16]. This arrangement yields more flexibility from the design and fabrication perspectives because the ring and the straight waveguides can be optimized separately. The thickness and material of the ring and waveguide can be modified according to the requirement. In the vertical coupling configuration, a nanometer-scale precision could be achieved in

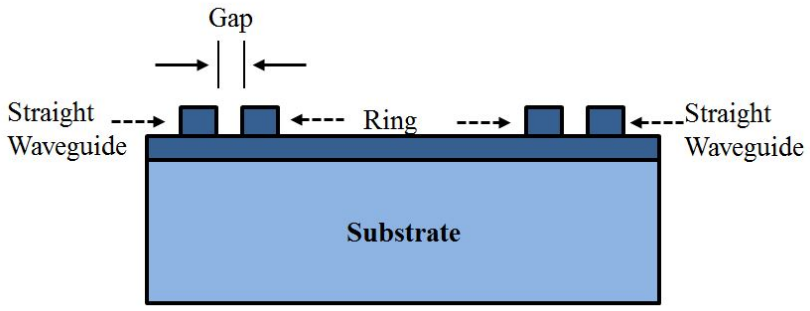

Figure 2.15: Cross section of the lateral coupling.

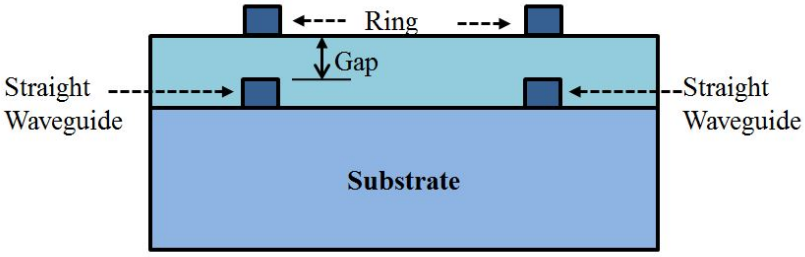

Figure 2.16: Cross section of the vertical coupling.

the process of deposition. However, as in vertical coupling scheme the materials for ring and waveguides are deposited in different layers, the alignment of them is a big challenge. Also, it is more difficult to achieve tapering in the vertical dimension, than in the lateral dimension.

2.4.5 Cascaded Microring Resonators

A promising approach toward the implementation of all-optical circuits is cascaded or higher-order microring resonators. Cascaded microring resonators consist of multiple rings coupled in a serial or parallel configuration. The parameters of each microring resonators and the coupling between ring resonators and input-output waveguides give the degrees of freedom to be used in the design to tailor the device characteristics to the required specification. These devices have shown promise in optical networks as

temporal differentiators [61,62], high-speed modulators [63], optical comparators [64], filters and sensors [65]. The cascading allows the fabrication of higher order filters with increased FSR compared to a single ring resonator device. In both serial and parallel structure the additional feedback paths result in an improved filter response, *i.e.*, a more flat-top response in the pass-band and a steeper roll-off at the pass-band edges. By higher order filter response, we refer to the spectral response or the roll-off compared to a single resonator device.

Fig. 2.17 (a) shows the schematic model of a serially cascaded microring resonator. Several microrings are placed between the input and output straight waveguides. At the resonance, the input light from the straight waveguide couples to the first ring, and the energy builds up as the light makes multiple round trips in the rings. A portion of light gets coupled to the second ring and the rest of the ring cascade in the same manner before coming out from the drop port. As the light has to travel sequentially through all the rings, all resonators must be precisely resonant at a common wavelength, which requires them to be identical. This makes the fabrication of serially configured microresonators more challenging.

In parallel configuration [Fig. 2.17 (b)], the rings are positioned one after another in such a way that all of them are connected by the same straight waveguides. A signal in the parallel configuration passes through all the ring resonators simultaneously, and unlike serial configuration here all the rings don't need to be identical. That is why, this configuration has less sensitive fabrication tolerance compared to serially cascaded configuration. The filter response of the parallel configuration depends on the length (Λ) of the bus waveguide between the rings (see Fig. 2.17). The distance Λ is chosen so that the transfer functions of each ring resonator add in phase [66]. By considering each microring is identical Λ can be determined by using the following formula:

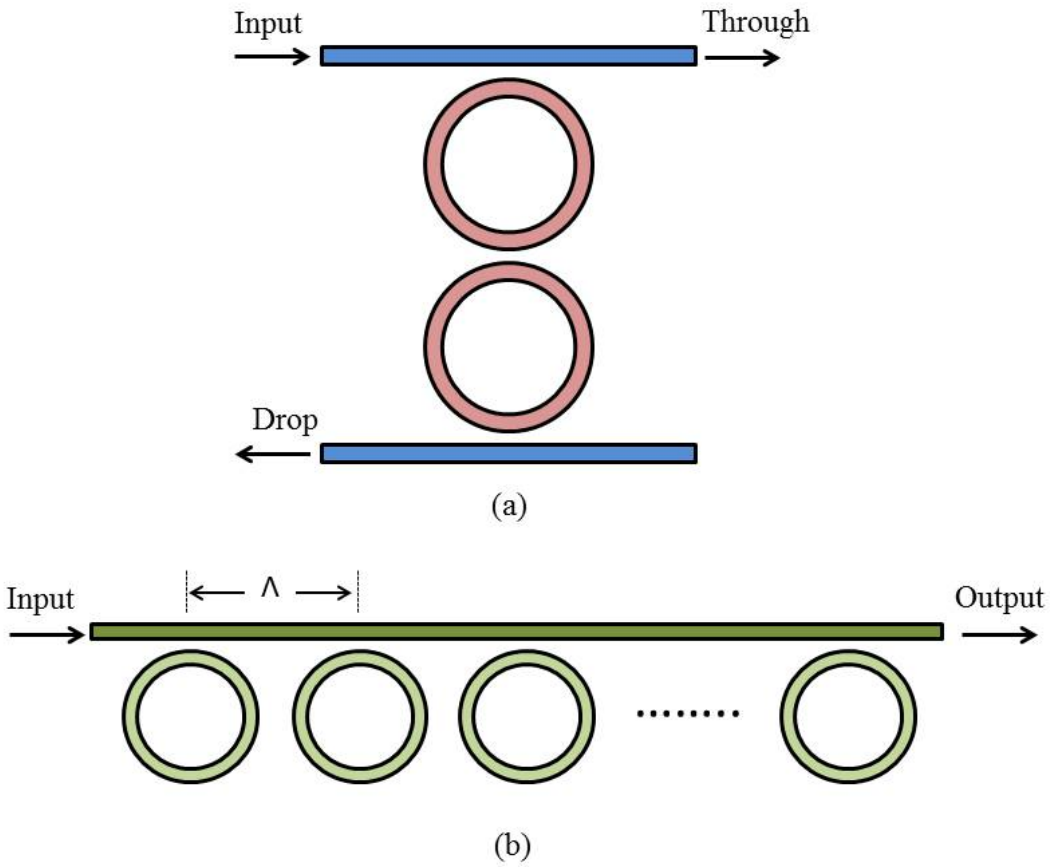

Figure 2.17: Schematics of higher order microring resonators with (a) serial and (b) parallel configuration.

$$\Lambda = \frac{m\lambda_{\text{res}}}{2n_{\text{eff, sw}}} \tag{2.30}$$

where, λ_{res} is a resonant wavelength, m is an integer, and $n_{\text{eff, sw}}$ is the effective refractive index of the straight waveguide.

Chapter 3

Nonlinear Effects and All-Optical Signal Processing

3.1 Nonlinear Optical Effects

The optical nonlinearity in semiconductor materials open the opportunity of bridging the functionality gap between optics and electronics. When an optical signal with a sufficiently high intensity is launched into an optical medium, the material response to such a signal becomes nonlinear. The nonlinear optical response of a medium can be described as a Taylor series expansion of the polarization $\tilde{P}(t)$ with respect to the electric field strength $\tilde{E}(t)$ of the optical field interacting with the medium [67]:

$$\tilde{P}(t) = \epsilon_0[\chi^{(1)}\tilde{E}(t) + \chi^{(2)}\tilde{E}^2(t) + \chi^{(3)}\tilde{E}^3(t) + \cdots]. \tag{3.1}$$

Here $\chi^{(n)}$ is the n-th order susceptibility of the optical medium. Second order nonlinear susceptibility $\chi^{(2)}$ is responsible for the three-wave mixing effects such as the second-harmonic generation (SHG), sum-frequency generation(SFG) [68] and difference-frequency generation (DFG) [68]. The third-order nonlinear optical sus-

ceptibility $\chi^{(3)}$ gives rise to the intensity-dependent refractive index resulting in such effects as self-phase modulation (SPM), cross-phase modulation (XPM), and four-wave mixing (FWM) [69]. All these effects can be utilized to achieve all-optical signal processing. Below we concentrate on the most common effect that could lead to some all-optical signal processing functionalities; namely, four-wave mixing.

3.1.1 Four-Wave Mixing

Four-wave mixing (FWM) is a nonlinear optical phenomenon which can be used to realize many optical signal processing operations such as optical wavelength conversion [70], optical time division multiplexing [71] and demultiplexing [72], and others.

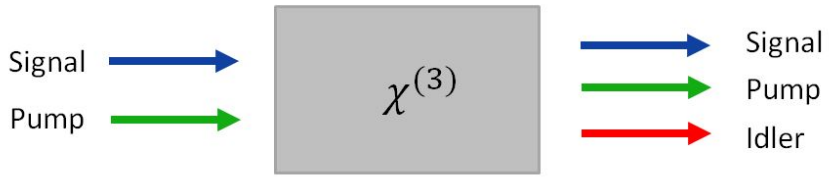

Figure 3.1: Schematic of the four-wave mixing effect in an optical $\chi^{(3)}$ medium.

FWM is a third-order parametric nonlinear optical effect. Fig. 3.1 shows the schematic of the four-wave mixing effect in an optical $\chi^{(3)}$ medium. Here, the input pump is produced by high power pulsed beams and the signal is a comparatively weak continuous wave (CW). For efficient FWM, the phase mismatch between the interacting waves must be nearly zero, which could be achieved, for example, if the pump is located around the zero-dispersion wavelength. When the phase matching conditions are met, two pumps photons interact with signal photon and give rise to a new frequency component known as idler. There are two types of FWM: degenerate and non-degenerate FWM (see Fig. 3.2). When the frequencies of the two pump photons

are identical, it is known as degenerate FWM. We will concentrate on considering the degenerate FWM for the rest of the thesis.

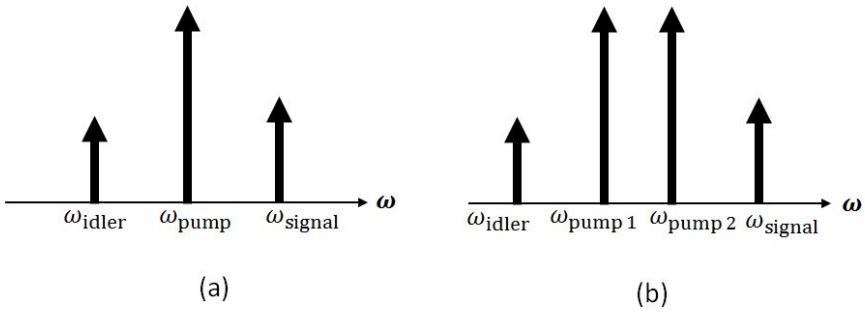

Figure 3.2: Schematic diagram of (a) degenerate and (b) non-degenerate FWM in the frequency. domain

For the degenerate FWM, the frequency of the newly generated idler can be found as follows:

$$\omega_{\text{idler}} = 2\omega_{\text{pump}} - \omega_{\text{signal}}. \tag{3.2}$$

3.1.2 Self-Phase Modulation

Self-phase modulation (SPM) is a nonlinear optical effect that describes the modification of the propagation conditions self-induced by a powerful beam of light. The light pulse traveling in a nonlinear optical medium induces a variation in the refractive index of the medium due to the *optical Kerr effect* which is a nonlinear change in the refractive index of a material due to the applied electric field. This variation in refractive index produces a phase shift in the pulse which leads to a change of the pulse's frequency spectrum.

The overall refractive index of the nonlinear optical medium acquires an intensity-dependent component and obeys the following expression [67]:

$$n(t) = n_0 + n_2 I. \tag{3.3}$$

Here n_0 represents the usual weak-field (linear) refractive index, n_2 is the non-linear refractive index (the material parameter that could be different for different optical media), and I is the pulse intensity. The variation in the refractive index results in a phase shift in that an optical pulse experiences as it propagates through the medium:

$$\phi_{\mathrm{NL}}(t) = -n_2 I(t)\omega_0 L/c. \tag{3.4}$$

This time-varying phase of the optical wave could lead to the spectral broadening [73–76] of the transmitted pulse. Also, when n_2 is positive, the leading edge of the pulse has the lower frequency components, and the tailing edge has the higher frequency components [67]. Figure 3.3 depicts the spectral broadening and frequency chirping due to the self-phase modulation when a signal and CW pump are injected in to a nonlinear medium.

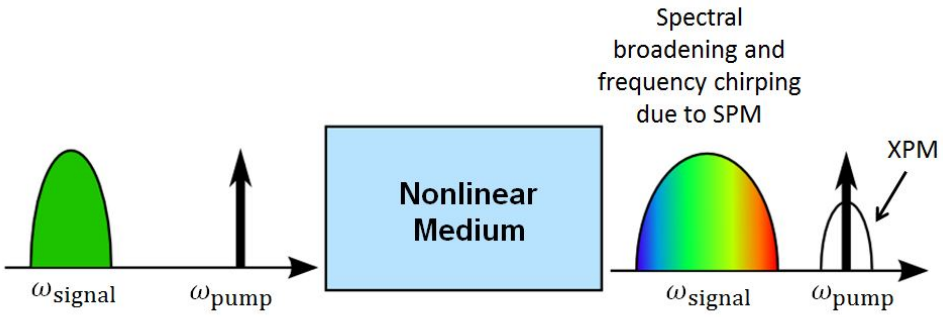

Figure 3.3: Schematic of self-phase modulation (SPM) and cross-phase modulation (XPM).

Recently SPM has received much attention because of its usefulness in optical switching [77] and supercontinuum generation [78]. However, the spectral broadening due to SPM can degrade the performance and could induce the modulation instability

that could increase the level of noise in the lightwave systems.

3.1.3 Cross-Phase Modulation

When two or more beams of different wavelengths propagate in a nonlinear medium simultaneously, the optical phase of one laser beam changes by interaction with another beam due to the optical Kerr effect. This nonlinear phenomenon is known as cross phase modulation (XPM). Cross-phase modulation is always accompanied by self-phase modulation (SPM) and it occurs because the effective refractive index seen by an optical beam in a nonlinear medium depends not only on the intensity of that beam, but also on the intensity of other copropagating beams [79].

The fiber nonlinearity can also couple two fields through cross-phase modulation (XPM) without inducing any energy transfer between them. The change in the refractive index (Δn_{NL}) induced by the third-order nonlinear optical effects is given by the equation [69]

$$\Delta n_{\mathrm{NL}} = n_2(|E_1|^2 + 2|E_2|^2). \tag{3.5}$$

Here E_1 and E_2 are two incident fields on the nonlinear optical medium. As the optical field propagates inside a nonlinear medium, it acquires an intensity-dependent nonlinear phase shift

$$\phi_{\mathrm{NL}}(t) = n_2(\omega/c)(|E_1|^2 + 2|E_2|^2)L. \tag{3.6}$$

Here, L is the length of the medium. The first term of Eq. 3.6 is responsible for the SPM, and the second term for XPM. The factor of 2 in the second term represents the fact that XPM is twice as large as SPM at the same level of intensity. Figure 3.3 illustrates the cross-phase modulation experienced by a CW pump due to the signal

pulse.

Cross-phase modulation has drawn much attraction in recent years due to its ability to control the signal via a nonlinear phase shift using a second pump light set at a different wavelength. XPM can be used to implement wavelength converters [80,81] and switches [82,83].

3.2 All-Optical Signal Processing

Nonlinear effects inside optical fibers and waveguides can be used for a high-speed processing of optical signals. Due to the recent advances in photonic integrated circuits, coherent detection of high speed system, access to four optical domains (amplitude, phase, polarization, wavelength), high-speed electronics and advances in materials, all-optical signal processing became the subject of intensive research. Ultrafast optical switching has been demonstrated as early as 1989 with the use of a nonlinear fiber-loop mirror [84]. All-optical signal processing allows us to avoid optical-to-electrical-to-optical (OEO) conversion, and to perform processing at the very high-speed line rate of optics, if the signals are already in the optical domain. Some examples of all-optical signal processing operations include optical wavelength conversion, optical time division multiplexing-demultiplexing, optical channel dropping, and regeneration.

3.2.1 All-Optical Wavelength Conversion

All-optical wavelength conversion is an important aspect of signal processing. The optical signal is allowed to remain in the optical domain throughout the conversion process. The wavelegth conversion can be implemented either by second-order nonlinear interactions resulting in a sum-frequency generation followed by a difference-frequency generation (SFG/DFG) [70] or by third-order effects, such as cross-phase

modulation (XPM) or four-wave mixing (FWM) [85].

To explain how four-wave mixing can be used for wavelength conversion, we assume that a modulated laser beam with the frequency ω_s carries a bit stream of data. This signal is synchronized with a non-modulated pulse stream with the frequency ω_p. Then this these two beams interact and produce an idler beam with a new frequency ω_i according to the four-wave mixing process (see Section 3.1). Whenever the bit of the signal sequence is "1", a "1" bit at ω_i is generated. Whenever the bit of the signal channel is "0", there is no radiation at ω_i, or 0 bit is generated (see Fig. 3.4). This process resembles the "AND" logic gate: if we mix "1" with "0", we will get "0"; if we mix "1" with "1", we will get "1". The output of this process is the reproduction of the original signal bit sequence at the new idler frequency, which means the signal is now converted to a new wavelength. Then we can filter out the signal and pump and transmit the idler bit sequence.

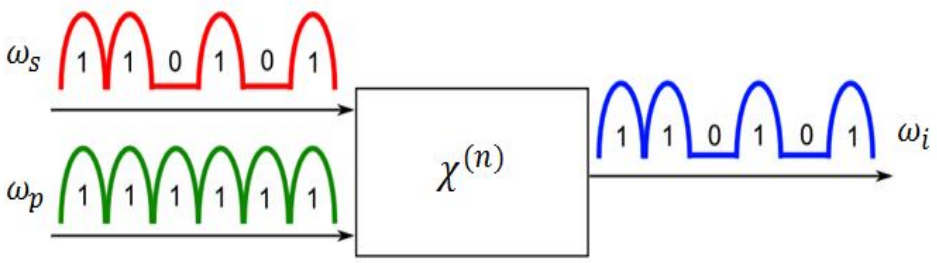

Figure 3.4: Wavelength converter based on nonlinear wave-mixing effect.

All-optical wavelength conversion enables ultra-high-speed all optical multiplexing-demultiplexing of WDM channels, channel adding, extraction, and regeneration.

3.2.2 Optical Time Division Multiplexing and Demultiplexing

Optical time division multiplexing-demultiplexing allows several channels to be transmitted or received by a higher bit-rate channel but in different time slots. We explain below how OTDM could be realized through the FWM process.

Let us consider three lower-bit channels which need to be multiplexed. To achieve the multiplexing, we need two extra non-modulated pulse streams. One of the non-modulated pulse streams should contain pulses with high repetition rate, corresponding to the bit rate of the multiplexed stream. Another non-modulated channel carrying higher-power optical pulses will be used to set up a temporal frame. The time difference between the two consecutive pulses in this channel should be long enough to fit three low-bit-rate information channels.

Time delay lines are needed to offset the all three information channels and to synchronize their bits with the pulses of the high-repetition-rate dummy (non-modulated) channel. Such temporal delay lines can be realized with the help of an optical fiber [86] or by means of ring resonators [87,88]. After passing through the delay lines, the three channels should be mixed with the non-modulated high-repetition-rate pulse and the higher-power framing pulse (see Fig. 3.5). The optical delays should be such that, the first bits of the first, second and third channels overlap in time with the three consecutive pulses of the high-bit-rate stream, respectively. Then the fourth pulse of the high-repetition-rate stream should overlap in time with the non-modulated framing pulse. If the four-wave mixing between the interacting channels and the two dummy pulse streams is efficient, an optical AND gate can be realized, resulting in the multiplexing of the three channels into a higher-bit-rate stream (see Fig. 3.5).

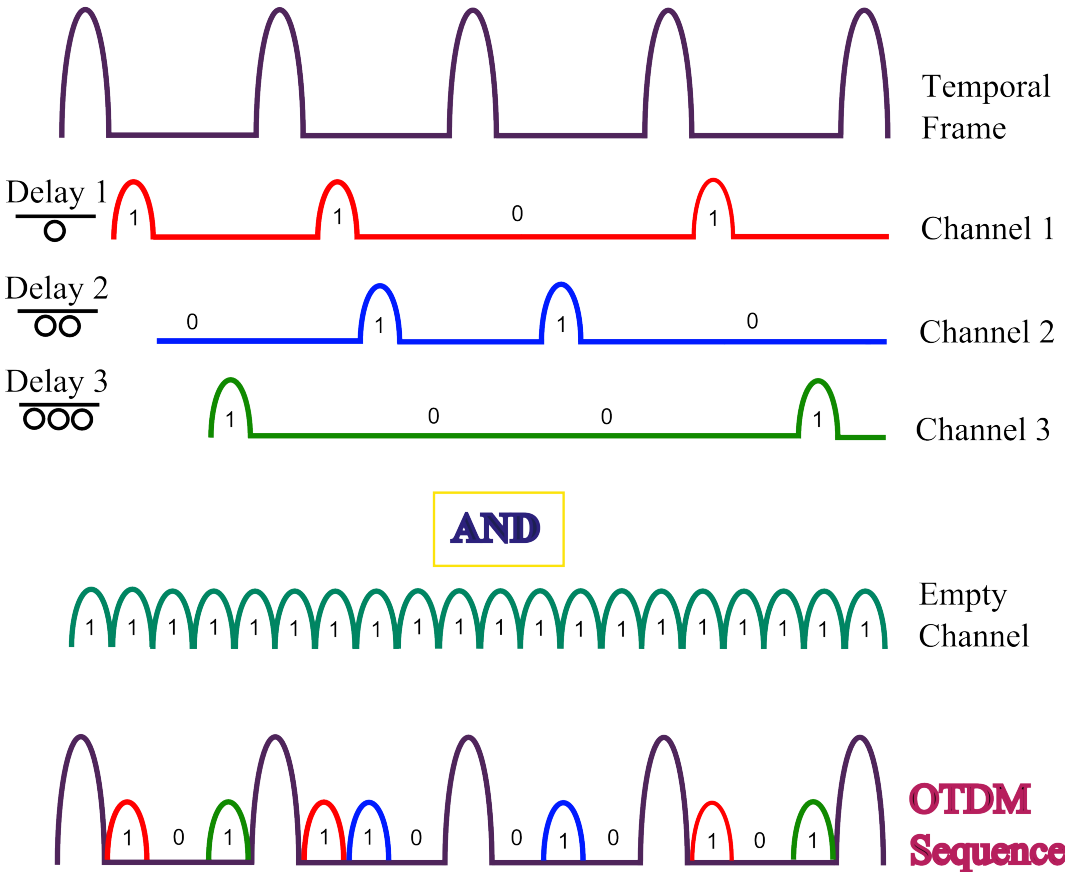

Figure 3.5: Four-wave mixing between the information channels and two non-modulated pulse streams resulting in the multiplexing of the three channels into a higher-bit-rate stream [89].

Chapter 4

Design of Microring Resonators and Numerical Results

In this chapter, we describe how we approach the design of our microring resonators, and present the results of the numerical analysis. In our study, we focused on the laterally coupled microring resonator configuration where the straight waveguides and ring are positioned in the same plane. All the numerical simulations were done using a commercial software package called *Lumerical MODE Solutions* which is a design environment for the analysis and optimization of integrated optical waveguides, components, and fibers.

4.1 Material Composition

As the first step in our design, we define a material composition of the AlGaAs wafer that is going to be used for fabricating the microring resonators. The wafer represents an arrangement of AlGaAs layers with slightly different compositions. This would allow us to define a guiding layer with the highest refractive index, and to achieve the vertical confinement of light in this layer through surrounding it with the lower-

refractive-index claddings. Figure 4.1 shows the layered structure of the wafer. The waveguide structure is a three-layer arrangement formed by two claddings and the core, epitaxially grown on top of GaAs substrate. The composition of the guiding layer was chosen to be $Al_{0.18}Ga_{0.82}As$, as it has been shown in the earlier studies [44,46], this composition exhibits negligible two-photon and three-photon absorptions at 1.55 μm. The refractive index of $Al_{0.18}Ga_{0.82}As$ at 1.55 μm is 3.2813 [35]. The photons with the wavelength 1.55 μm have the energies lower than half the band-gap energy for $Al_{0.18}Ga_{0.82}As$. That is why, two-photon absorption for this material composition is negligible. The value of the two-photon absorption coefficient of $Al_{0.18}Ga_{0.62}As$ is $\alpha_2 = 0.05$ cm/GW [46]. The thickness of the guiding layer was set to 0.6 μm to minimize the effective mode area. We first describe the material compositions of the claddings, and then explain the choice of the waveguide dimensions.

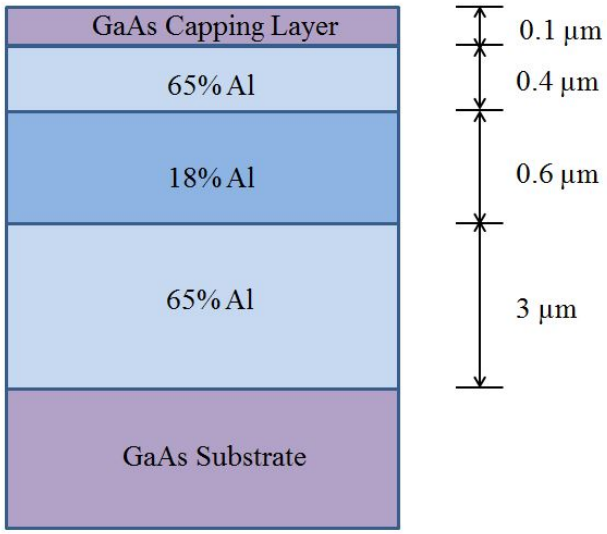

Figure 4.1: AlGaAs Wafer composition.

The upper and lower claddings were chosen to have 65% of aluminum in order to maximize the refractive index contrast between the core and cladding layers and to prevent oxidization. Even though the higher concentrations of aluminum result in the

lower values of the refractive index and even higher refractive index contrast with the guiding layer, AlGaAs with 70% of aluminum starts oxidizing very rapidly with time. The oxidation leads to an increase in the propagation loss and the loss of predictability of the device operation. That is why, we set the aluminum concentration to 65% to be on the safe side of the 70% limit. The refractive index of $Al_{0.65}Ga_{0.35}As$ is around 3.046 at 1.55 μm, which results in the refactive index contrast of $\triangle n \approx 0.24$. The high index contrast between the claddings and core is necessary to maximize the light confinement in the core layer and to ensure that there is no light leakage to the GaAs substrate which has the highest refractive index of all layers. The thickness of the upper cladding was set to 0.4 μm. We have also used 3 μm thick lower cladding to isolate the mode and to prevent its leakage to the substrate. The entire structure was capped by a thin 100 nm layer of GaAs to prevent oxidation. The wafer has been grown by CMC Microsystems, Canada, as designed.

4.2 Design Criteria for Microring Resonators

The first step was associated with the design of the waveguide cross section for the microring resonators. Once the key waveguide cross-section has been designed, we proceeded to the next step of designing the microring resonators themselves. Our goal was to design ring resonators optimized for four-wave mixing process. The software package Lumerical Mode Solution was used to perform the design. The Eigenmode Expansion (EME) solver and 2.5D variational FDTD (varFDTD) solver of Lumerical MODE Solutions make it a complete package to simulate passive optical waveguides and fibers. We performed our design simulations using these solvers based on the following criteria.

- **Single-mode operation:** we know that the light propagating through a waveguide can take multiple paths along the medium. The number of paths it can

take depends on the waveguide dimensions and the refractive indices of the core-cladding layers. The different paths that the waveguide is capable of supporting correspond to different stationary electromagnetic field distributions within the core of the waveguide. These field distributions represent different modes. The lowest-order mode is called *fundamental mode*. The fundamental mode takes the shortest path and experiences the lowest propagation loss in the waveguide. Because of these reasons our goal was to design the waveguide cross section of our microring resonators in such a way that they can support a single fundamental TE and TM mode.

- **Free-spectral range (FSR):** FSR is the difference in wavelength between any two consecutive resonance peaks. It is inversely proportional to the cavity length of the ring resonator [see Eq. (2.15)]. The limits on the value of the FSR are dictated by a specific application. For example, in DWDM systems the channel separation should be 100 GHz. It means that, if we were to design a microring resonator compatible with a DWDM system, we would have to make sure that FSR = 0.8 nm. In our proof-of-principle studies, we select FSR to have the values of 5 nm and more to ensure that the peak separation is sufficient for the detection and analysis.

- ***Q*-factor:** In order to demonstrate efficient nonlinear optical interactions, a microring resonator should have a large Q-factor. To maximize the Q-factor, it is important to reduce the losses in the cavity. The three main loss mechanisms that contribute to the total round-trip loss are the propagation loss, bending loss, and coupling loss. Eq. 2.23 suggests that larger cavity length L can lead to a higher value of the Q-factor. On the other hand, the overall propagation loss increases with the increase of the cavity length. An optimization has to be performed to find the proper balance between the values of these two parameters

that could lead to the highest values of the Q-factor.

4.3 Design and Results

The parameters responsible for the optical performance of a microring resonator include its coupling length, the radius of the ring, the gap between the ring and straight waveguide, and the waveguide dimensions. These parameters have been identified in the process of the design. One can directly relate FRS, resonant wavelength, and Q-factor to the optical performance of the device in general. Another important factor that we need to keep in mind while designing microring resonators is fabrication tolerances. There are certain challenges associated with the process of fabricating microring resonators (such as, *e.g.*, achieving a sufficient etching depth, especially in the gap region). As a result, one needs to take into consideration of possible deviations of the actual device parameters from the ones set in the design. Also, one has to set some tolerances within which the device is still expected to perform its functions. We have found from the simulations that etching 0.4 μm into the 3 μm lower cladding should be sufficient in order to achieve a stable modal pattern in all parts of the device, and in order to prevent the light from leaking to the substrate. With the 0.4 μm of etching into the lower cladding, taking into account the dimensions of the upper cladding and the guiding layer, the overall etching depth should be 1.5 μm (see Fig. 4.2).

The design of microring resonators mainly involves designing straight waveguides and rings. But to make the microring resonators functional, the tapers and wider coupling waveguides are also required to make large input laser beams compatible with the smaller core of the microring resonators. Fig. 4.3 illustrates the main components of a functional microring resonator.

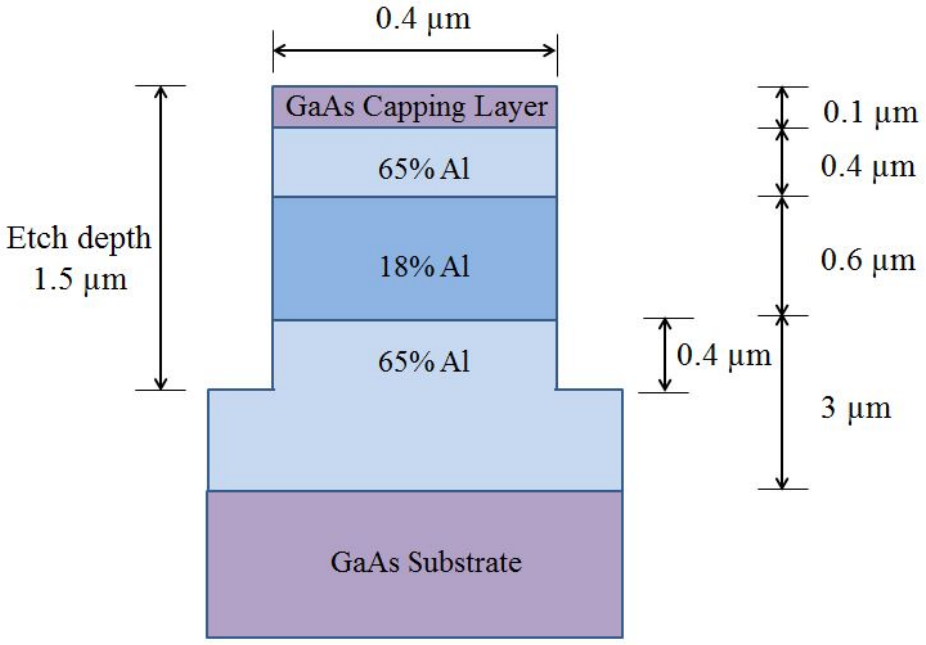

Figure 4.2: Schematic of the waveguide dimensions.

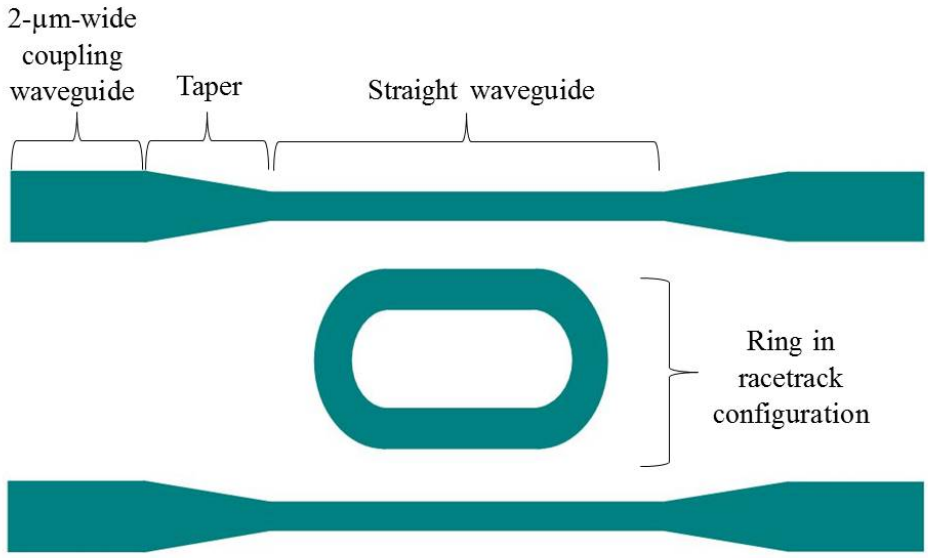

Figure 4.3: Tapered AlGaAs microring resonator.

In the following sections, we present the design of the waveguide cross-section used in the microring resonators. Then the overall design process, the analysis and the results are presented. At the end, the design of the taper which efficiently converts

the mode size of the input beam to the size of the waveguide core is discussed.

4.3.1 Modal Analysis

The Finite Difference Eigenmode (FDE) solver by the Lumerical MODE solutions calculates the spatial profile and frequency dependence of the waveguide modes by solving Maxwell's equations on a cross-sectional mesh of the waveguide [90]. The solver calculates the mode field profiles, their effective refractive indices, and estimates their losses due to the bends in the design and material absorption. The later does not include the actual scattering losses characteristic to a fabricated device due to imperfections. In addition, an integrated frequency sweep can be used to calculate the group delay, dispersion, effective mode area, and other parameters associated with the light propagation through the device.

We started out by creating the materials for the core ($Al_{0.18}Ga_{0.82}As$), claddings ($Al_{0.65}Ga_{0.35}As$), and substrate (GaAs) in the material database of the mode solver. The refractive indices for different material composition of AlGaAs were determined by Gehrsitz's analytical model [35]. For aluminum concentration x, the index of refraction (n) of $Al_xGa_{1-x}As$ is given by

$$n^2(x) = A(x) + C_0(x)/(E_0^2(x) - E^2) + C_1(x)/(E_1^2(x) - E^2) + R(x). \tag{4.1}$$

Here $R(x)$ is the reststrahl correction, given by the equation

$$R(x) = (1 - x)C_2/(E_2^2(x) - E^2) + xC_3/(E_3^2(x) - E^2). \tag{4.2}$$

In last two equations A, C_0 , C_1, E_0, E_1, and E are constants determined empirically. The constant A represents the contribution to the dielectric function of the highest energy transitions. The constants C_0 , C_1, and C_2 are associated values of three

resonant energies E_0, E_1, and E_2.

Based on the core and claddings dimensions, and the deep-etch nature of the waveguide cross-section of the microring resonators, in order to achieve a single-mode operation in these devices, the waveguide width should be less than 1 μm. Such AlGaAs waveguides have been termed "AlGaAs nanowires" [91,92]. In order to analyze the characteristics of the microring resonators, such as their effective index, group delay, dispersion, we first created a simple nanowire structure (Fig. 4.4). Then the mode field profiles of the TE and TM modes (Fig. 4.5) of a straight AlGaAs waveguide of the width 0.4 μm were obtained using FDE solver. It can be seen from Fig. 4.5 that the field profiles of the TE and TM fundamental modes are slightly different. The effective modal area of the TE mode is around 0.226 μm^2, and the effective modal area of the TM mode is around 0.359 μm^2 for a waveguide with the width 0.4 μm. The amount of the total power confined within the guiding layer portion of the waveguide is around 86% and 81% for the TE and TM modes, respectively.

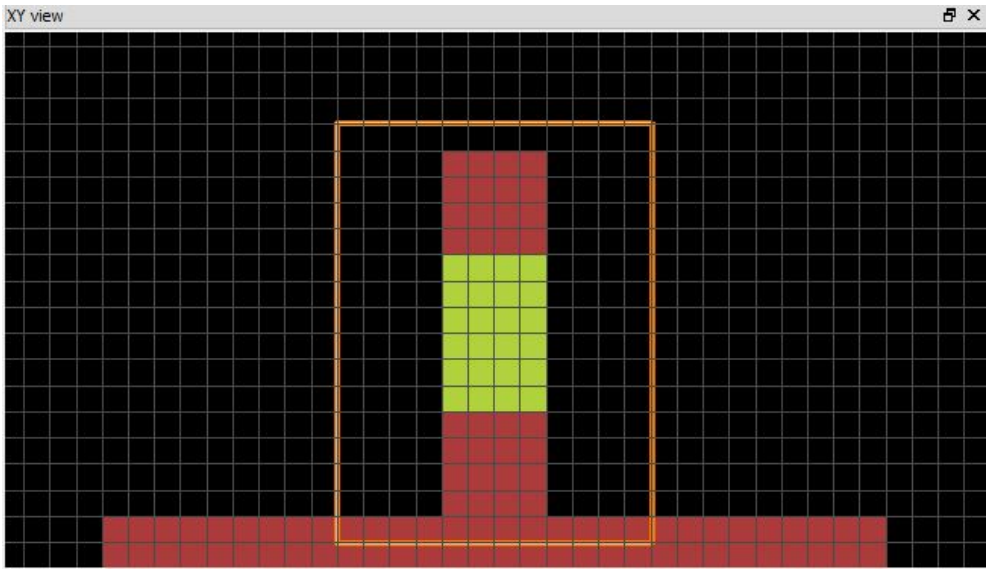

Figure 4.4: Simulation layout of the waveguide.

As can be concluded from Eq. (2.4), the values of the effective refractive indices

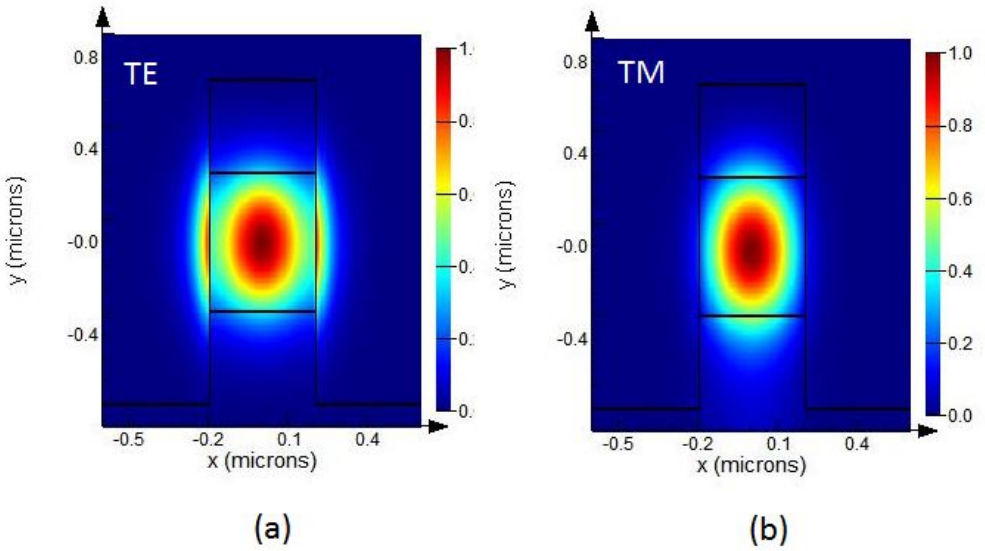

Figure 4.5: Intensity distribution of fundamental (a) TE mode and (b) TM mode of a straight AlGaAs waveguide of width 0.4 μm.

(n_{eff}) of the microring resonator modes play an important role in determining their resonant wavelengths. We plot these characteristics as the functions of wavelength in Fig. 4.6 for the fundamental TE and TM modes.

The light transfer between the input waveguide and the ring takes place in the coupling region. Here, the most critical feature is the gap between the ring and straight waveguide which controls the coupling strength. Generally, the narrower gaps result in better coupling efficiency. In Fig. 4.7, we show the cross section of the transfer region with a gap of 100 nm. It resembles two coupled waveguides: one is the straight waveguide (on the left-hand side), and the other is the ring cross section (on the right). The waveguide mode appears to be a little bit shifted towards the gap region, as compared to the mode profile of a single waveguide (see Fig. 4.5). The overlap in the evanescent tails of the modes, leading to the power transfer between the straight waveguide and the ring can be observed. The effect of the gaps on the operation of the microring resonator is discussed in more detail in Section 4.5.3.

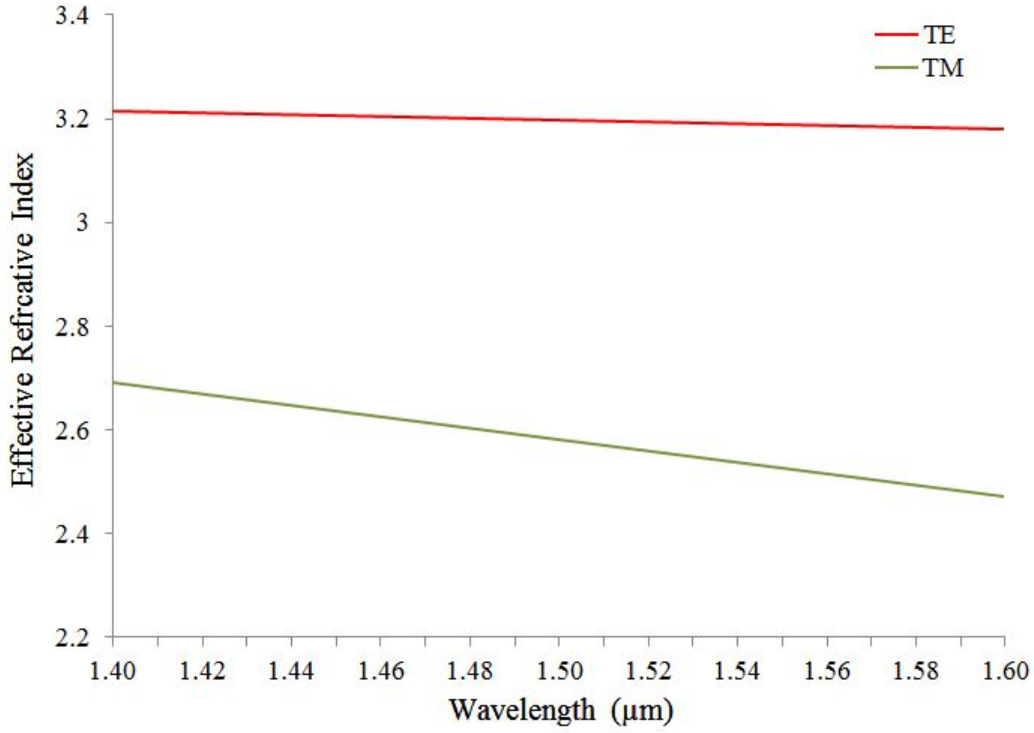

Figure 4.6: Effective refractive index (n_{eff}) of the fundamental TE and TM mode as a function of wavelength.

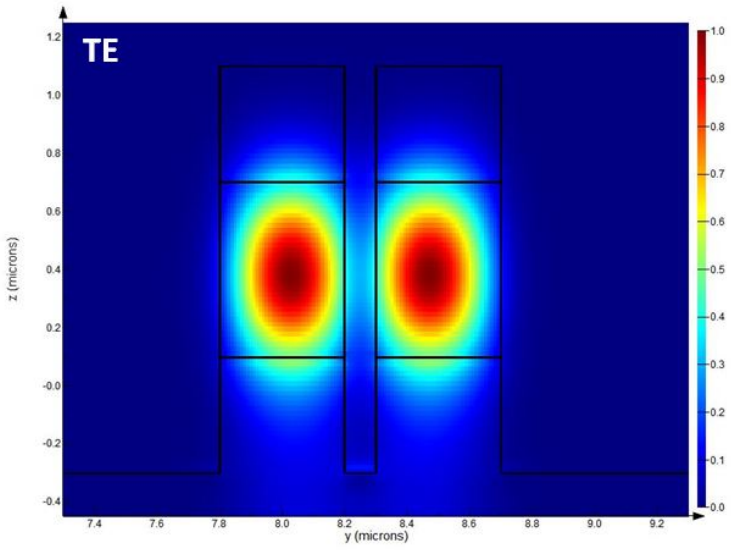

Figure 4.7: Intensity distribution of the fundamental TE mode in the coupling region.

4.3.2 Dispersion Analysis

Dispersion is the dependence of the optical response on the wavelength of light. This includes the material characteristics, such as the refractive index, dielectric permittivity, susceptibility, and, as a consequence, group velocity, which are, in general, the functions of wavelength. In addition to the material dispersion affecting the aforementioned material parameters, there are other types of dispersion typical for guided waves as they propagate through a waveguide. These include intermodal dispersion (that appears in multimode waveguide structures only) and waveguide dispersion that appears as a consequence of the partial confinement of the overall modal field in the waveguide core.

Group velocity dispersion (GVD) is a characteristic of a dispersive medium which determines how the medium will affect the duration of an optical pulse traveling through it. It causes a short pulse of light to spread in time due to the fact that different frequency components of the pulse travel at different velocities. The GVD has two contributions coming from the material dispersion and waveguide dispersion. The definition of the group velocity v_g is

$$v_g = (\mathrm{d}\beta/\mathrm{d}\omega)^{-1}, \tag{4.3}$$

where $\beta = \bar{n}k_0 = \bar{n}\omega/c$ is the propagation constant and $\bar{n}$ is the effective index at the operating wavelength. The dispersion parameter D in an optical waveguide is related to the group-velocity dispersion parameter β_2 (where $\beta_2 = \mathrm{d}^2\beta/\mathrm{d}\omega^2$) through the following expression:

$$D = \frac{\mathrm{d}}{\mathrm{d}\lambda}\left(\frac{1}{v_\mathrm{g}}\right) = -\frac{2\pi c_o}{\lambda^2}\beta_2. \tag{4.4}$$

Here, v_g is the group velocity. The β_2 determines how much an optical pulse would

broaden on propagation inside the waveguides. The dispersion of the fundamental TE and TM modes of an AlGaAs waveguide is calculated using Lumerical MODE solutions (see Fig. 4.8). The zero dispersion wavelength for the TE mode of our designed waveguide is around 1.55 μm, whereas the TM mode exhibits normal dispersion in this wavelength range.

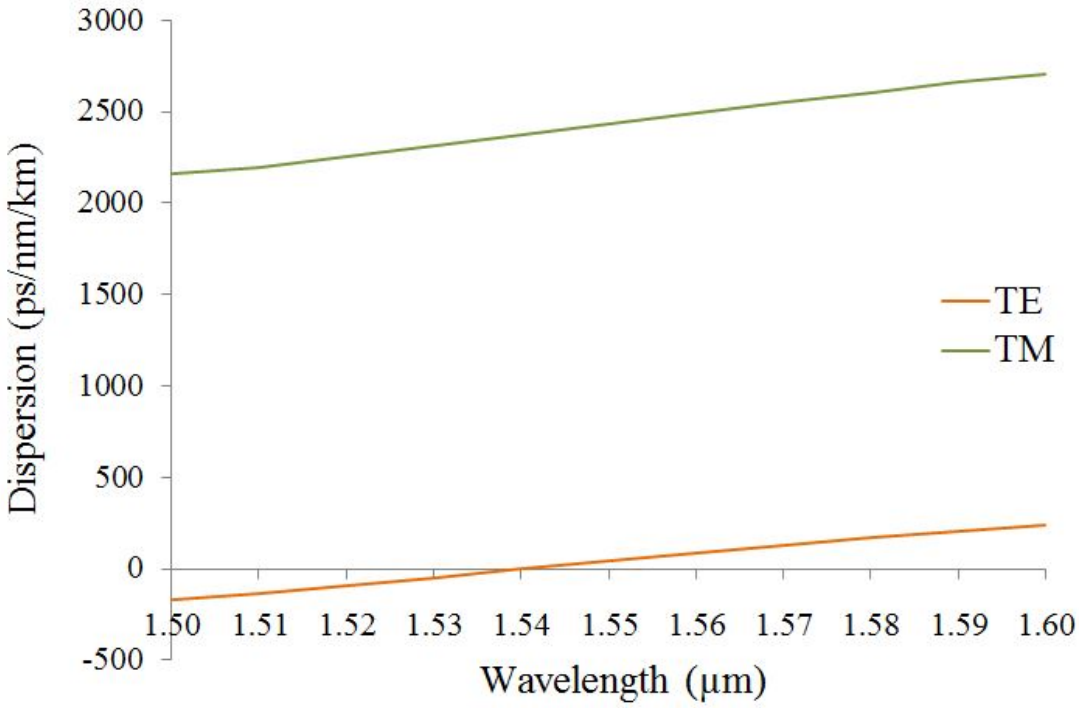

Figure 4.8: The dispersion characteristics of the fundamental TE and TM modes of an AlGaAs waveguide. The waveguide has the width 0.4 μm, the core ($Al_{0.18}Ga_{0.82}As$) thickness 0.6 μm, the upper cladding ($Al_{0.65}Ga_{0.35}As$) thickness 0.4 μm. The total thickness of lower cladding is 3 μm where the etch depth goes 0.4 μm into the lower cladding.

4.3.3 Transmission Analysis

The analysis of transmission characteristics of microring resonators is an important step that gives useful information about their FSR, Q-factor, and resonances. We use the varFDTD method for the transmission analysis. The propagator allows for planar

(omni-directional) propagation without any assumptions about an optical axis, which allows for structures like ring resonators and photonic crystal cavities to be efficiently modeled. It provides faster broadband modeling of linear and nonlinear phenomena in waveguide systems as compared to the traditional FDTD method.

Using the same materials that we added to the Lumerical material database for the modal analysis (Section 4.5.1) as the core, cladding ans substrate layers, we defined microing resonators in racetrack structure in MODE solutions. The structure is depicted in Fig. 4.9 which shows the layout of the simulation window.

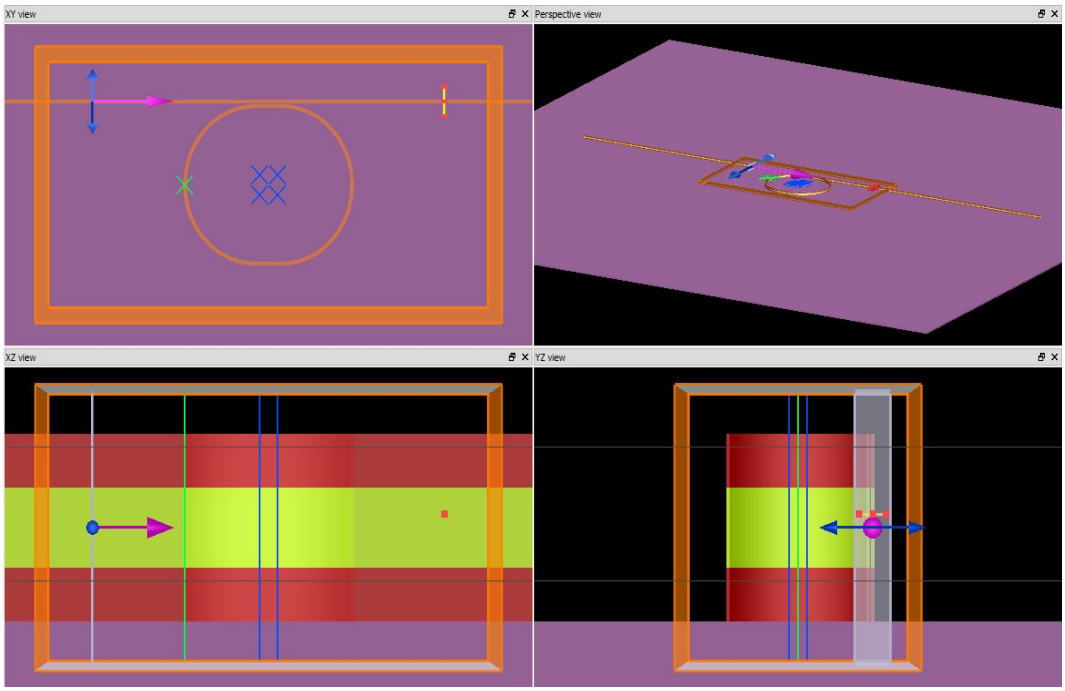

Figure 4.9: The layout of the microring resonator simulation in Lumerical MODE solutions.

The simulations were carried out for both all-pass and add-drop resonator structures. The broadband transmission data were obtained form the through and drop waveguides for different values of the ring radius, coupling waveguide length, waveguide width and the gap between the straight waveguide and the ring (see Fig. 4.10).

The transmission spectrum of the through port of an all-pass ring resonator

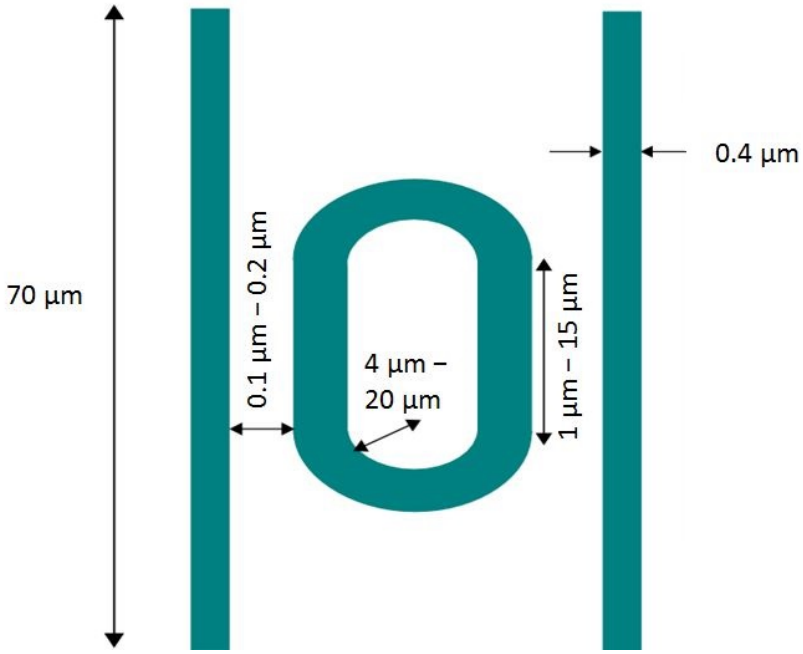

Figure 4.10: The schematic of the add-drop microring resonator with the parameter ranges specified on the drawing.

(waveguide width 0.4 μm, ring radius 8 μm, coupling length 3 μm and gap 0.1 μm) is presented in Fig. 4.11. The x axis represents the input wavelengths and the y-axis is the normalized output power. The drops in the transmission spectrum occur at the input wavelengths which satisfy the resonance condition of the microring. The input light with the wavelength corresponding to one of the resonances of the resonator gets coupled from the straight waveguide to the ring and stays inside the ring for a period of time, while the rest of the wavelengths travel out of the through port. One of the resonances of this structure coincides with 1.55 μm. At this wavelength, around 99.9% of the input light gets coupled to the ring.

To analyze the transmission characteristics of add-drop microring resonators it is necessary to measure the output power at both the through and drop ports. In add-drop resonators the wavelength of light which satisfies the resonant condition gets coupled to the ring and completes several round trips inside the ring before coming out from the drop port (see Fig. 4.12), whereas the wavelengths that don't

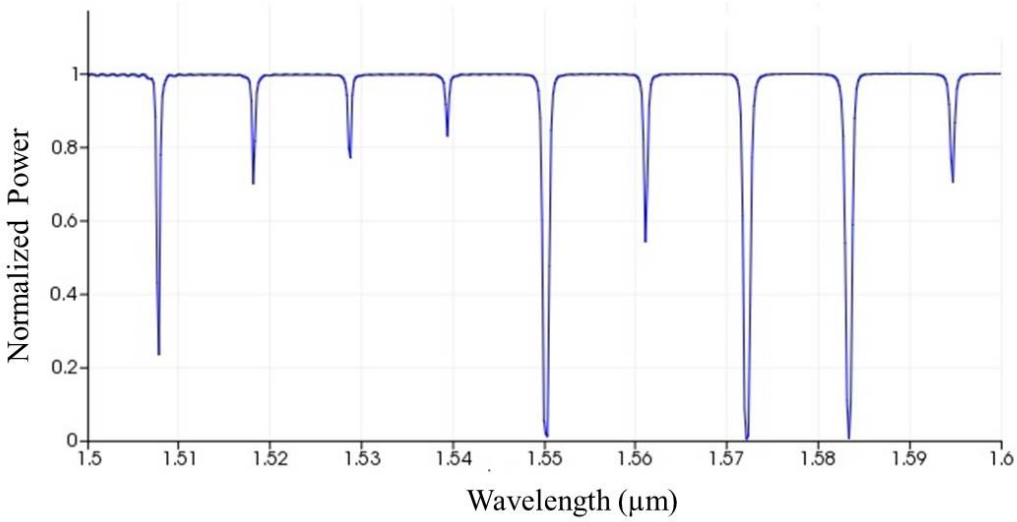

Figure 4.11: Transmission spectrum at the through port of an all-pass ring resonator. The radii of the half rings are 8 μm, coupling length and the gap between straight waveguide and coupling waveguide are 3 μm and 0.1 μm, respectively. The widths of all the waveguides are 0.4 μm.

satisfy the resonant condition come out straight form the through port. In such a way, the transmission spectra of the through and drop ports exhibit deeps and peaks, respectively. Fig 4.13 displays such transmission spectra of both thorough and drop ports of an add-drop microring resonator. The radii of the half rings of this racetrack microring resonator is 5 μm, the length of the coupling region is 3 μm, and the gap width between the coupling-in waveguide and the ring is 0.1 μm. Both spectra show dips and peaks at the resonant wavelengths, as expected. For example, at the wavelength 1.55 μm, 92% of the input optical power gets coupled to the ring in the coupling region. Out of this 92%, only 5% of the power gets lost in the ring, and the rest (87%) comes out of the drop port.

In Table 4.1, we summarize our simulation results for different ring radii, gap widths, and coupling region dimensions. Here the width of all the waveguides and rings are 0.4 μm, as other widths resulted in worse transmission characteristics. In the table, we show the percentage of the optical power that makes it into the ring, and

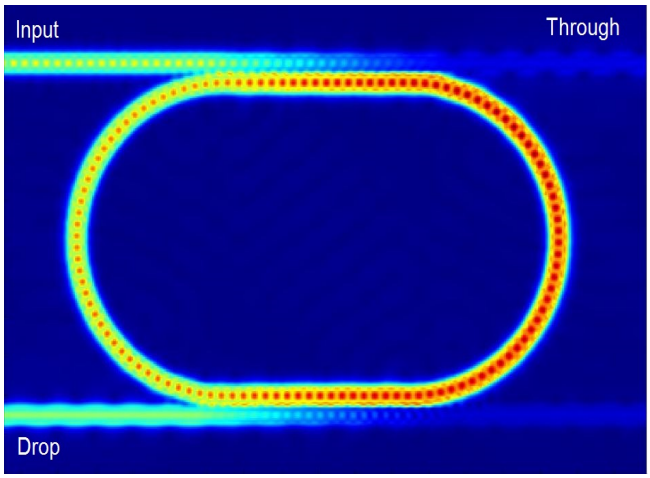

Figure 4.12: Finite difference time domain (2.5D FDTD) simulation demonstrating the optical power build-up at 1.5567 μm in a microring resonator. The ring radius is 4 μm, the coupling length is 5 μm and the gap between the straight waveguide and coupling region of the ring is 0.1 μm. The widths of both straight waveguide and ring are 0.4 μm.

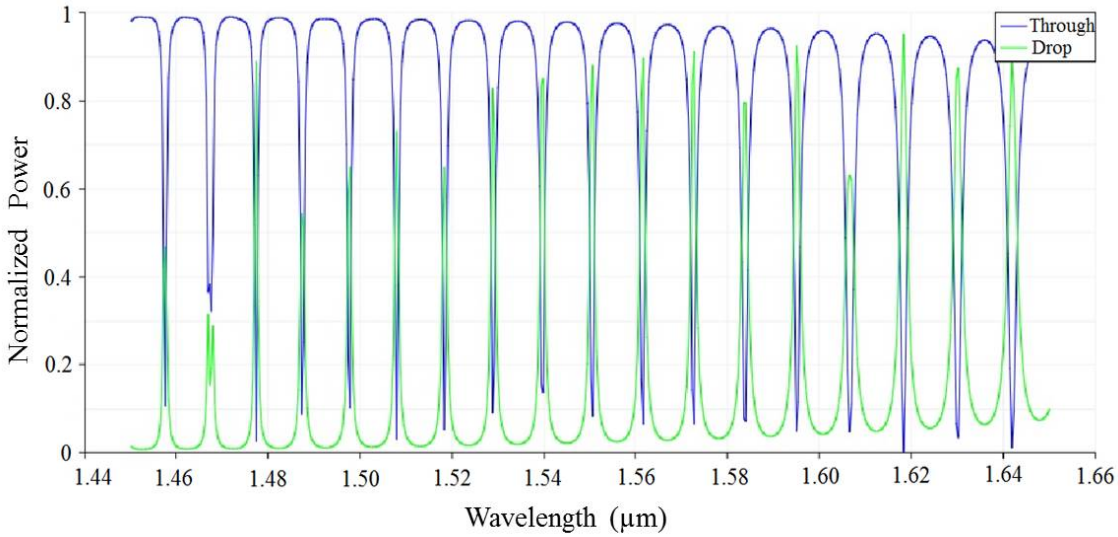

Figure 4.13: Transmission spectra of the through and drop ports of an add-drop ring resonator. Here, the radii of the half rings are 5 μm, the coupling length and the gap between the straight and coupling waveguides are 3 μm and 0.1 μm, respectively. The widths of all the waveguides are 0.4 μm.

the percentage of the optical power that comes out of the drop port. The difference between these two values signifies the power lost in the microring resonator for the

reasons such as bend losses. This excludes the estimate of the power lost because of the device imperfections and scattering.

Radius (μm)	Coupling length (μm)	Gap (μm)	Coupled input power to the ring (%)	Power at drop port (%)
4	3	100	97	75
4	5	100	99	92
4	10	150	100	86
5	2	100	85	46
5	3	100	92	87
6	10	150	99	81
8	3	100	93	59
9	3	100	96	70
10	7	150	92	55
12	3	100	95	56
20	5	100	99	97
20	5	150	97	73

Table 4.1: The coupled power to the ring and power at the drop port for different radii of the half rings, coupling lengths, and gap widths between the straight waveguide and ring. The resonant wavelength around 1.55 μm was selected. Here, the width of all the waveguides is 0.4 μm, as other widths resulted in worse transmission characteristics.

The strong light confinement in the optical waveguide dictates that the resonator-to-waveguide gap has to be very small for adequate evanescent coupling. To investigate how the gap width affects the coupling, we plotted the normalized power at the though port and normalized peak power at the drop port as functions of the gap width at the resonant wavelength of 1.55 μm for a ring resonator with the radius 8 μm, coupling length 7 μm, and waveguide width 0.4 μm (see Fig. 4.14). The "Through" represents the fraction of input power that doesn't get coupled to the ring and comes out of the through port. For the 80-nm gap, almost 0% input power at

1.55 μm reaches the through port. As the gap increases, this value increases and less power gets coupled to the ring. The normalized power that reaches the drop port is represented by the "Drop" curve in the plot. It decreases drastically as the gap increases.

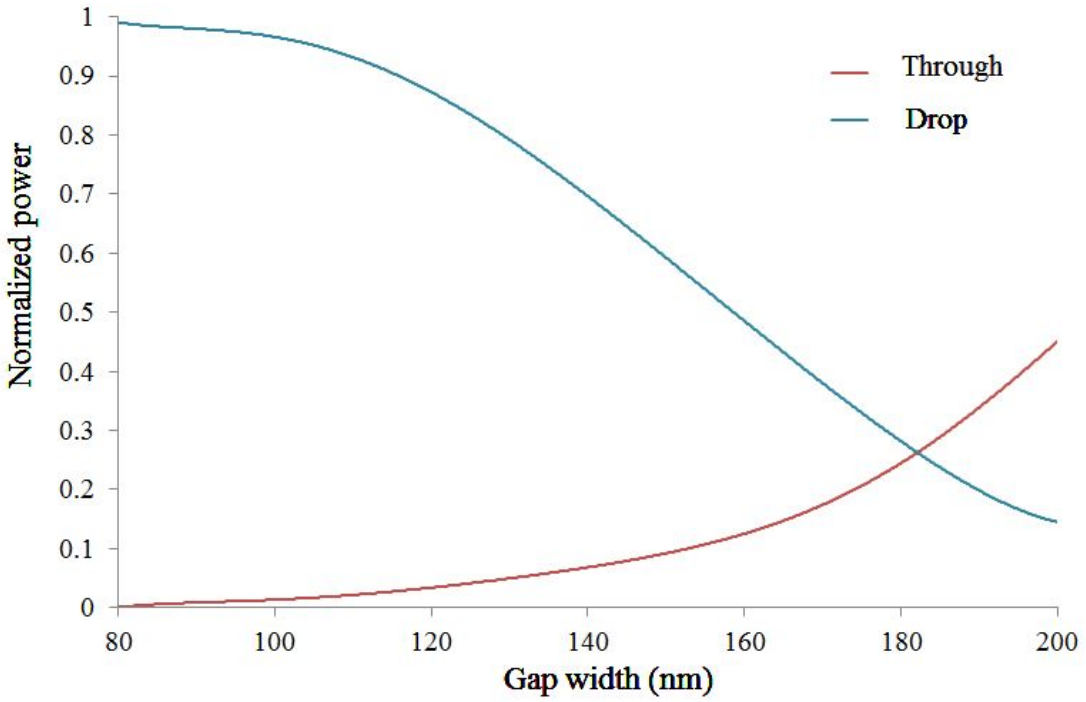

Figure 4.14: The value of the normalized transmitted power at the through and drop ports at the resonant wavelength around 1.55 μm of a microring resonator as a function of the gap width between the straight waveguide and the ring. The ring resonator has a racetrack structure. The radii of the half rings are 8 μm, and length of coupling region is 7 μm.

4.3.4 FSR and Q-factor

FSR and Q-factor describe the performance and characteristics of a resonator. Recall that, FSR is the spacing between two successive transmitted optical intensity maxima or minima of a spectrum, and Q-factor is defined as the ratio of the operation wavelength and the FWHM of the resonant peak. These two parameters are discussed in detail in Section 2.3.

The FSR of a microring resonator depends on the size of the ring. It is also related to some other factors such as the resonant wavelengths and effective refractive index (n_{eff}). Different applications require different values of FSR. For example, in a WDM system, 0.4, 0.8 or 1.6 nm FSR is needed to fit in more wavelength channels and to achieve a higher data bandwidth [93, 94]. So, for this system a larger microring resonator is required. Fig. 4.15 shows the plot of FSR as a function of the total round trip length of an AlGaAs racetrack microring resonator at the wavelength 1.55 μm. The waveguide core dimension is 600 nm $\times$ 400 nm. The FSR of a microring resonator is equal to or more than 5 nm for round trip length of less than 140 μm. For example, the round trip length a microring resonator with 4 μm radius of the ring and 3 μm coupling length is 24.2 μm and the FSR of this microring resonator is 28.9 nm.

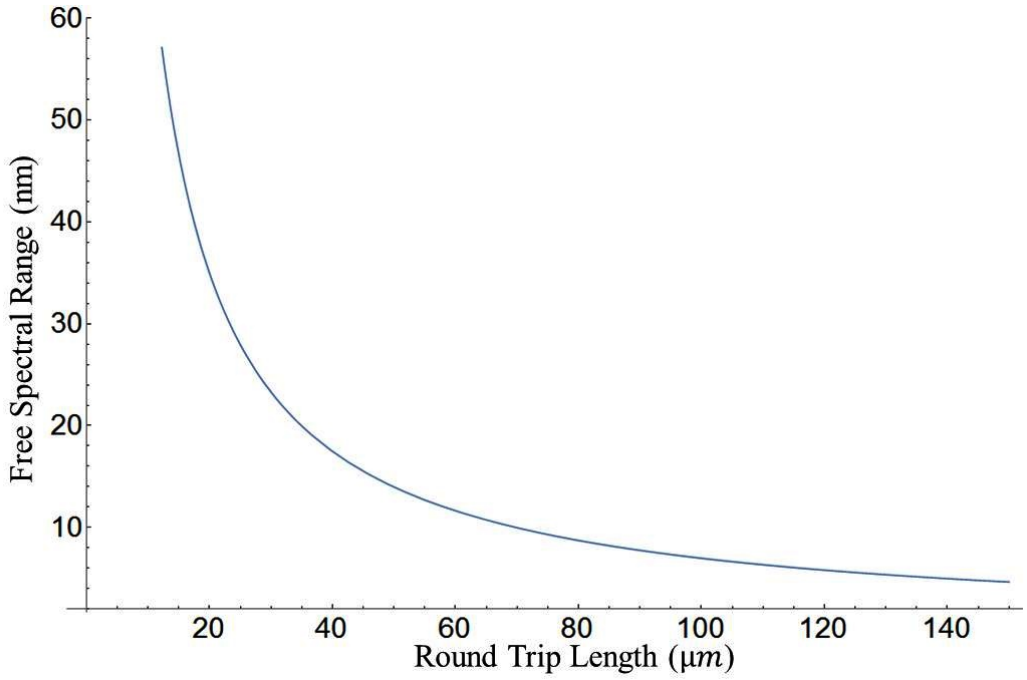

Figure 4.15: Calculated FSR (in nm) as a function of the round trip length (in μm) of an AlGaAs microring resonator at the wavelength 1.55 μm . Here, the radius and coupling length vary with the round-trip length, and the width of the waveguides is set to 0.4 μm.

In order to ensure a high value of the Q-factor, it is important to minimize the losses in the cavity. For a racetrack resonator structure, along with the ring, we also have to consider the excess bend losses due to the modal mismatch at the straight-bend transition. The losses in the coupling section originate from the propagation, from additional sidewall roughness affecting the distributed intensity, and from other imperfections caused by the fabrication process. The formula for the Q-factor (Eq. 2.22) suggests that a higher Q is achievable for large cavity lengths. However, the accumulated propagation loss also increases with the cavity length. An exponential increase in the Q-factor is generally expected to occur with the increase of the ring length upto a certain limit. After that the Q-factor reaches a plateau at larger round trip lengths. In our calculations we ignored the bending loss as the bending loss is low for high index waveguides. With the propagation losses set to 5.7 dB/mm (the typical experimental value for a moderate-quality AlGaAs nanowire waveguide for the fundamental TE mode at 1.55 μm [92]) and $t \approx 0.99$ we have plotted Q-factor as a function of the round trip length (μm) of AlGaAs microring resonators (see Fig. 4.16). In the beginning the Q-factor increases sharply. However, as the round-trip length increases, the Q-factor reaches a plateau due to the accumulated propagation loss. For our designed composition a highest Q-factor of approximately 10400 could be achieved.

4.3.5 Four-Wave Mixing Simulation

One of our targets for designing ring resonator is to observe nonlinear four-wave mixing (FWM) effect which can be used to realize many optical signal processing operations such as optical wavelength conversion [70], optical time division multiplexing [71] and demultiplexing [72], *etc.*

The process of FWM has been described in Section 3.1.1. To simulate this phe-

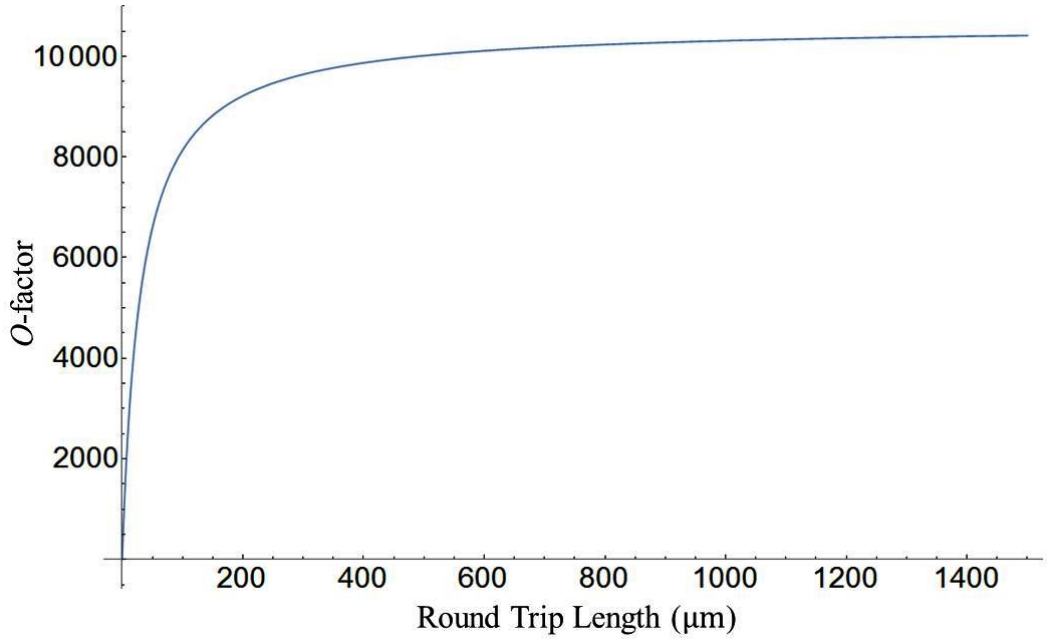

Figure 4.16: Calculated Q-factor as a function of the round trip length (μm) of AlGaAs microring resonators. Here, the propagation loss of the waveguide is set to 5.7 dB/mm.

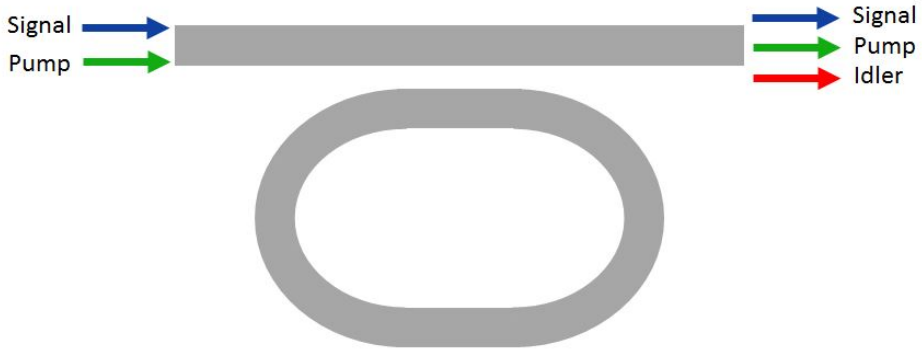

Figure 4.17: The schematic of the four-wave mixing in an all-pass microring resonator.

nomenon, we selected two resonant wavelengths of a ring resonator with the radius 8 μm and coupling length 3 μm. One resonant wavelength is 1.554 μm which we used as the wavelength of the pump, and as the signal we used a source with 1.588 μm wavelength. Both of these sources are transmitted to the input port of our selected

microring resonator (see Fig. 4.17). The power of the pump is higher than the power of the signal. Both wavelengths interact while propagating through the ring resonator and produces an idler. In Fig. 4.18, showing the transmission spectrum at the through port, it can be seen that an idler is formed at the wavelength 1.521 μm at the through port.

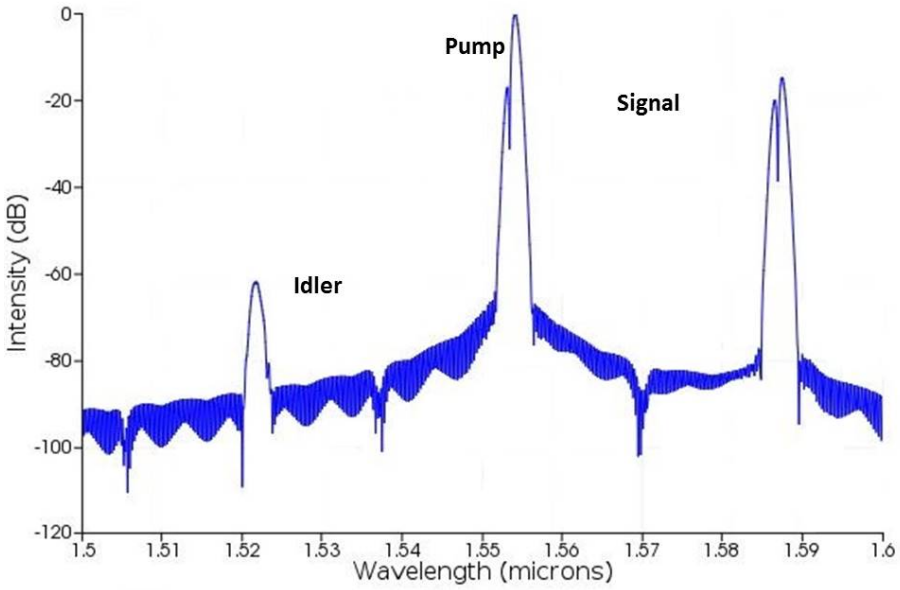

Figure 4.18: Simulation result showing generation of idler at 1.521 μm by a 1.554 μm pump and 1.588 μm signal.

4.4 Tapers

Since the core dimensions of the nanowire waveguide are less than a micron, in order to achieve efficient coupling by a direct focusing of the laser source onto the waveguide cross-section, measures need to be taken to increase the amount of light coupled into the device. A spot-size conversion is essential for making larger laser beam compatible with the smaller core of the microring resonators.

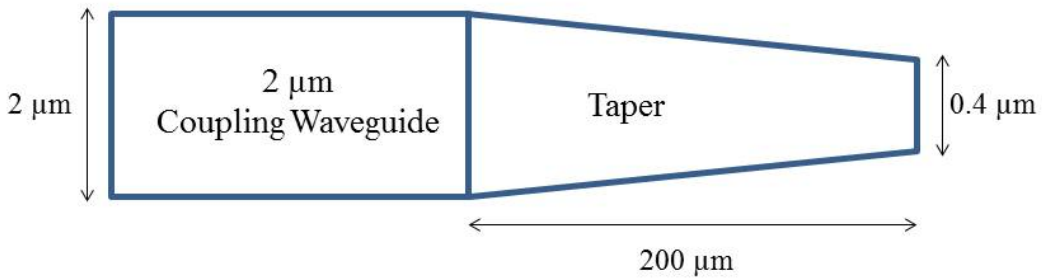

Figure 4.19: The top view of the structure and dimension of the spot-size converter used to taper down the input beam into the straight waveguide of our designed microring resonator.

To simplify coupling in and out from the devices, we start with a 2 μm wide coupling waveguides at the input to the devices, followed by tapers reducing the waveguide dimension down to the width of the nanowire, and then expanding it again at the output to 2 μm. Studies by our group members show that a 200-μm-long taper can provide a low-loss spot-size conversion down to the dimensions of the nanowire [no reference]. The top view of the taper with all its dimensions is shown in Fig. 4.19. Fig. 4.3 shows the arrangement of the coupling waveguide and taper with the designed microring resonator.

Chapter 5

Fabrication of AlGaAs Microring Resonators

The fabrication techniques for AlGaAs integrated optical devices have already been well established [95, 96]. This is one of the reasons why AlGaAs is an attractive candidate for photonic integration. Also, recent advances in nanofabrication have made it possible to fabricate AlGaAs structures with the dimensions on the order of tens of nanometers. An overview of the fabrication process is discussed in this chapter. This chapter also summarizes our attempts to fabricate the microring resonators devices and the insights gained in the process.

5.1 Fabrication Process

The first step of the nanofabrication process involves growing a vertically layered structure known as wafer (see Fig. 4.1) which would be the base material for the integrated optical devices. There are mainly two techniques to grow III-V semiconductor wafers: molecular beam epitaxy (MBE) and metalorganic chemical vapour deposition (MOCVD). In MBE process, the growth on a heated substrate in ultra-high vacuum

(UHV) environment is done using elemental sources. Where as, MOCVD is a chemical vapor deposition method used to produce single or polycrystalline thin films. The schematic of the fabrication process is illustrated in Fig. 5.1. Once the wafer is ready, the waveguide structures with a 2D confinement are ready to be defined on top of it using lithographic fabrication techniques. For that, a photoresist (for photolithography) or electron-sensitive resist (for e-beam) mask layer is formed on top of the wafer. There are two types of resists: positive and negative. In case of negative resist, the resist areas exposed to the light in photolithography (or electron beam in electron beam lithography) become insoluble when immersed in the developer. The unexposed portion of the negative resist is dissolved by the developer. In case of positive resist, the portion that is exposed to light or electron beam becomes soluble when immersed in the developer, and the portion that is unexposed remains insoluble to the developer.

As the next step, the desired waveguide patterns are created on top of the resist layer using lithography processes. In this thesis, we will only discuss the electron beam (e-beam) lithography process. The e-beam lithography is a specialized technique where a focused beam of electrons is used for creating extremely fine patterns on a surface covered with an electron-sensitive resist. This process is also known as exposure. The dose test is an important step during the exposure to determine the appropriate amount of charge and time necessary to expose the resist.

After the exposure, the sample is typically immersed in a liquid developer to dissolve the fragments (in the case of positive resist) or non-crosslinked molecules (in the case of negative resist). Depending on the type of resist, different chemicals are used to amplify the reactions, which are triggered during exposure.

Next step is the etching process where the unprotected areas (areas without the resist layer on top) are removed and the waveguides are formed according to the patterns created during the e-beam. There are two types of etching techniques: wet

etching and dry etching.

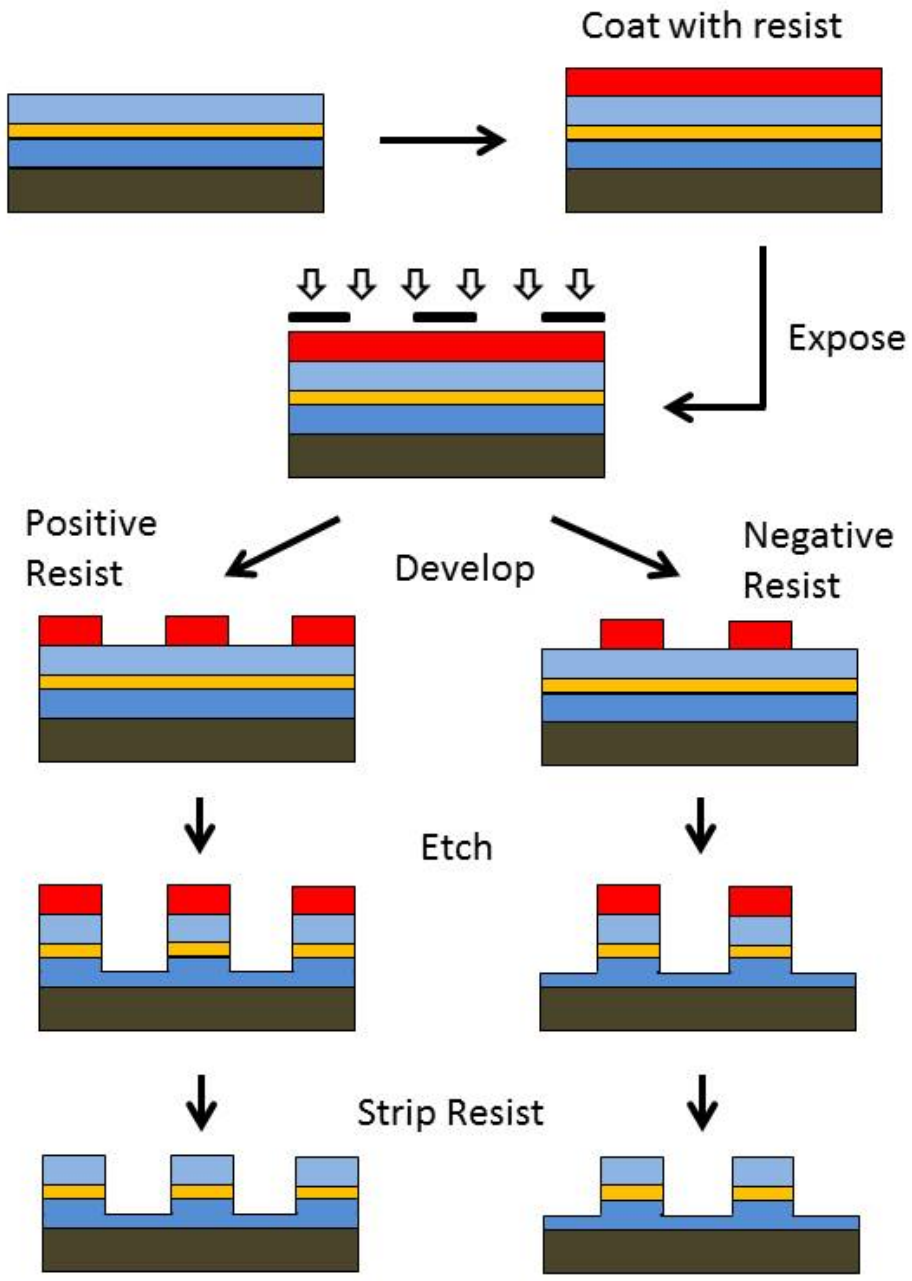

Figure 5.1: Steps of the fabrication process.

Wet etching process uses liquid chemicals or etchants to remove materials from the wafer. In dry etching, plasmas or etchant gasses are used remove the wafer material. The reaction that takes place can be done utilizing the high kinetic energy of particle beams, chemical reaction, or a combination of both. The wet etching process is usually isotropic where the etch rate is same both horizontally and vertically. The isotropic process produces round sidewalls. The dry etching is usually an anisotropic process where the etching occurs only in single direction and produces vertical sidewalls. During etching the concentration of the chemicals, the chemical reactions, and temperature can affect the etch rates.

In the last step of the fabrication process, the resist layer is striped off from the sample and the device is then ready to be used.

5.2 Fabrication of Microring Resonators

As the first step to fabricate the microring resonators, the AlGaAs wafer (see Fig. 4.1) was grown by CMC Microsystems, Canada. The Molecular beam epitaxy (MBE) process was used to grow the wafer on top of a GaAs substrate. We decided to use the MBE process for our wafer as it produces high quality wafer with less defects. After the wafer was grown, a part of it was used by our group to fabricate straight waveguides. Preliminary experiments show that the fabricated straight waveguides support the fundamental mode and perform as expected.

The fabrication of the microring resonators is challenging because of its complex structure and extremely small gaps between the straight waveguides and the rings. The gap is the most critical feature as it has the smallest dimensions. Due to the defects associated with various steps of the fabrication process, the device parameters do not come out exactly as designed. So, it is important to consider the fabrication tolerances while designing the device.

As we didn't have an in-house fabrication facility when starting the project, we decided to outsource the task. Multiple attempts to fabricate the devices did not lead to the desired result because of the numerous difficulties at different facilities and the cost involved. We find it instructive to discuss the two fabrication efforts as we have learned many useful tricks for future from those attempts. The first attempt was very close to being successful and the insights we have gained from that process were implemented later on. The second attempt has just resulted in visually high-quality devices that are going to be experimentally tested in the nearest future, and will hopefully give us promising results.

The design for the first fabrication attempt was based on our simulation results. The sample layout contained racetrack add-drop resonators with the radii of the half rings 4, 8, 12, and 20 μm. The two half rings of each mircoring resonator were connected by coupling waveguides which were expected to enhance the coupling efficiency. The coupling lengths of 1 and 3 μm were used for the 4, 8, 12 μm half rings, and the coupling lengths 5 and 10 μm were used for the microring resonators with the 20-μm half rings. The targeted width of the waveguides was 0.4 μm, and the gap was 0.1 μm. Considering the fabrication tolerances, we also included the samples with the waveguide widths 0.35, 0.4, and 0.45 μm and the gaps of 0.08, 0.1, and 0.12 μm in our design. Zhongfa Liao and Pisek Kultavewuti from Professor Aitchison's group from the University of Toronto helped us with the e-beam pattern writing and the development process.

A 200-nm-thick layer of 1:2 HSQ:MIBK solution was deposited on top of the wafer. This thickness of the resist layer is suitable for developing a 100-nm gap. The HSQ (hydrogen silsesquioxane) is a negative resist, and it is popular for e-beam lithography due to the fine resolution achievable ($\sim$10 nm) [97]. The thickness of the coated resist also plays a major role in the achievable resolution. After exposing the surface of the resist using e-beam lithography the sample was developed. Fig. 5.2 shows the SEM

(scanning electron microscope) image of one of the microring resonators from the sample after it has been developed, and Fig. 5.3 shows a fragment of the sample containing microring resonators photographed under the optical microscope.

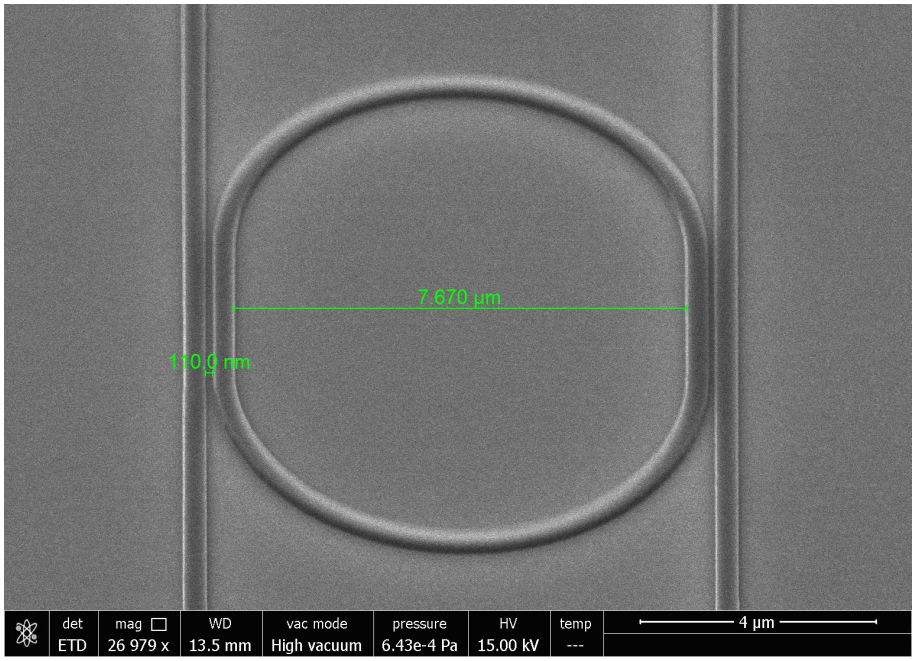

Figure 5.2: SEM image showing a microring resonator after the development.

After the e-beam exposure and development, the etching was performed by Kashif Awan from our group at the Cornell Nanofabrication Facility (CNF) using ICP-RIE (inductively coupled plasma and reactive-ion etching) process. First, etch tests were done using waveguides with different gaps in between to find out how the waveguide structure and gaps turn out. Fig. 5.4 (a), (b), and (c) show the SEM images of the gaps between two waveguides 80, 100, and 120 nm apart, respectively. A lot of surface roughness on the etched waveguides is clearly visible in the images. Excessive sidewall roughness leads to severe scattering losses which reduce the transmission. Also, the etch rate was very low within the gaps and it was not possible to achieve the etch depth as per the design. As the gaps get larger, the etch depth within the gap increases, but it is still smaller that required by the design, and the waveguide sidewalls are not

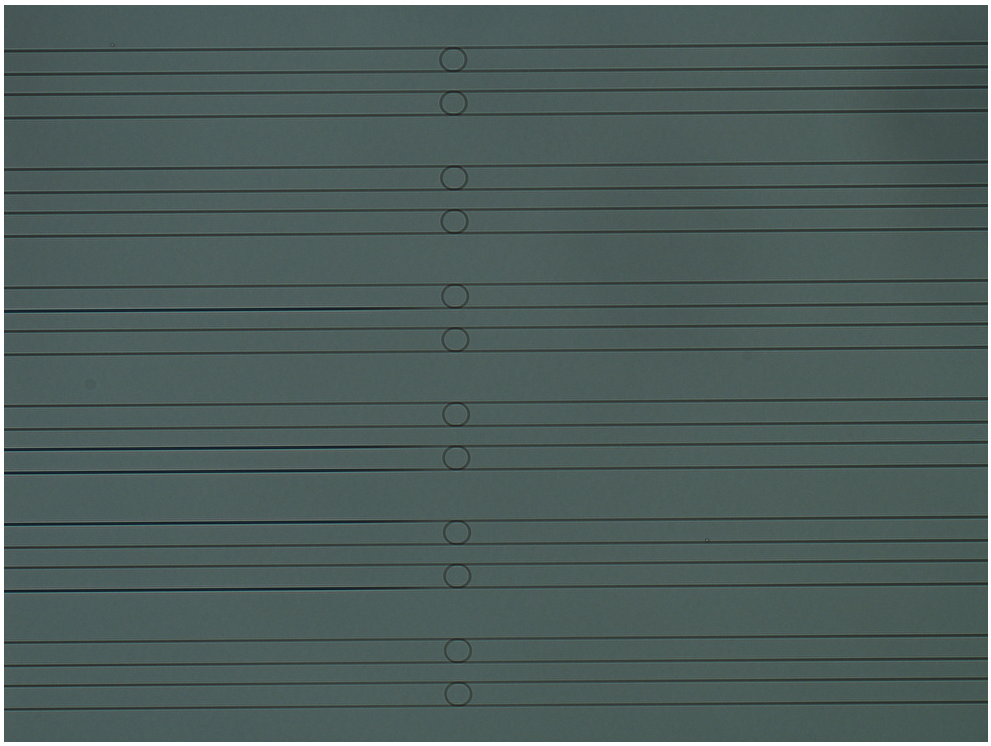

Figure 5.3: A fragment of the sample containing microring resonators photographed under the optical microscope.

straight, exhibiting the inclination angles of approximately 60°. Fig. 5.4 (d) shows an SEM image of a 2-μm-wide waveguide. Despite of some surface roughness, the waveguide sidewalls are vertical. Due to the errors of the fabrication process the 2 μm ridge width came out as 2.261$\pm$0.01 μm. This set of microring resonators didn't guide light through them. We think this happened due to the excessive surface roughness after the etching, and because the gaps were not etched through to the designed depth. Excessive sidewall roughness leads to severe scattering losses which reduce the transmission and finesse down to non-practical values.

From this process we have learned that in order to get the desired results, we need to develop a high etch rate recipe, which is possible only with chlorine. But this process requires passivation, *e.g.* nitrogen, to avoid side wall roughness, which was not available at CNF. At the same time we also need to reduce aspect ratio (the ratio

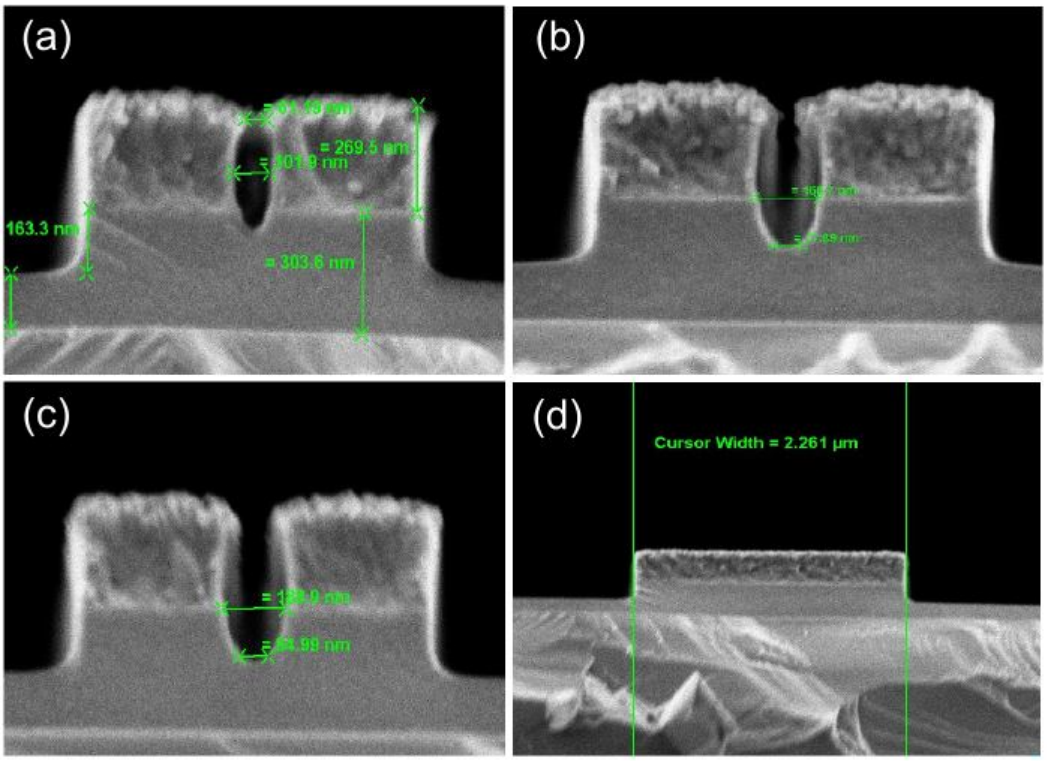

Figure 5.4: SEM images of two waveguides which are (a) 80 nm, (b) 100 nm, and (c) 120 nm apart. (d) SEM image of a straight waveguide with the width 2 μm.

of the height of the etch to the gap between the waveguides) by increasing the width of the gap.

For our next attempt, we designed a sample which includes both all-pass and add-drop ring resonators. Previously we faced difficulties in fabrication due to the very small gap size, so, we included a few devices with 200-nm-gaps between the ring and straight waveguide in the new sample layout. Based on our simulation results, waveguides and rings with the widths 0.4 μm worked the best for our wafer composition. In order to make sure that we have some alternatives in case if fabricating 400-nm-wide waveguides turns out to be a challenge, we also added some waveguides and rings with the widths 0.55 μm, 0.7 μm, and 1 μm . The width 0.7 μm has already proven to work for AlGaAs microring resonators with similar wafer composition [98]. This sample was fabricated at the University of Waterloo nanofabrication facilities with

the help of Professor Aitchison's group from the University of Toronto. The reason behind using the fabrication facilities of the University of Waterloo is that, they had nitrogen in their ICP-RIE etcher, which is required for high-etch-rate recipes. At first the wafer surface was prepared by removing organic contaminants and native oxide. Then FOX15: MIBK=1:1 was deposited on top of the wafer with the spinning speed 4000 rpm, acceleration 584 rpm^2, and spin duration of 60 seconds. This resulted in a 200-nm-thick resist layer on top of the wafer. After that, the sample was baked on a hotplate at 80°C for 4 minutes. Then the exposure and development were performed. After testing different doses to find out the optimum charge and time required for the exposure and development, we found that the 1400 $\mu C/cm^2$ dose with the development time 30 seconds was the best for the 400-nm waveguides with 80 nm gaps. The 1600 $\mu C/cm^2$ and 1800 $\mu C/cm^2$ doses worked best for the 120-nm and 200-nm gaps, respectively, for the same development time and waveguide width. Then the sample was rinsed with DI (de-ionized) water and soaked in isopropanol for about 10 seconds for easy dry up and removal of any residual. After the development, the sample was blow dried using N_2. Then the sample had undergone ICP-RIE etching using chlorine and nitrogen gas. At the end, the resist layer was stripped off from the sample using HF. Fig. 5.5 shows the SEM images of the etched sample. The images show low surface roughness, straight vertical walls and perfectly defined (200 nm) gap region. The sample was etched to the depth of 1.324 ± 0.01 μm from the top of the semiconductor material.

This sample is presently being tested for its optical performance. The preliminary experiments shows that the microring resonators with the widths 0.7 μm and 1 μm support the fundamental mode.

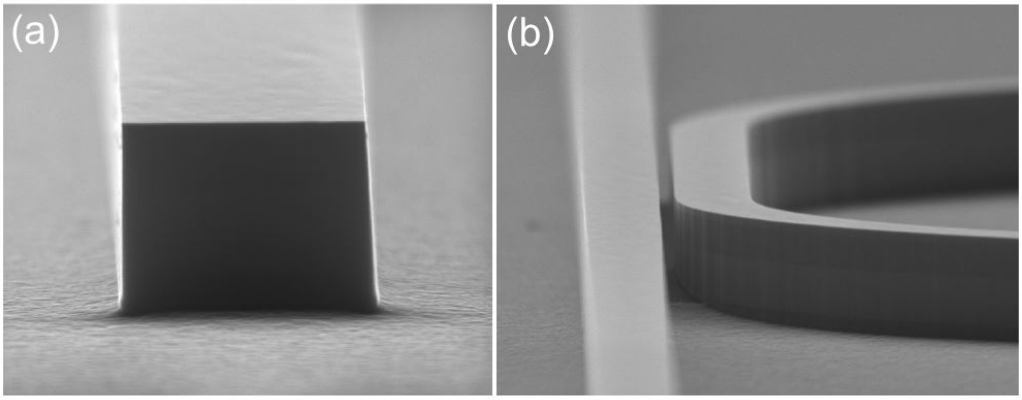

Figure 5.5: SEM images showing the etched (a) cross-section of the waveguide, and (b) a 200 nm gap between the ring and straight waveguide.

Chapter 6

Summary

The analysis of AlGaAs microring resonators optimized for optical four-wave mixing process has been presented in this thesis. Microring resonators with single-mode operation and high Q-factor are required to realize efficient nonlinear optical effects. Numerical calculations were done to design single-mode microring resonators with high Q-factors. The width of the waveguide which gives a single mode operation and the effective refractive indices of that waveguide for both TE and TM mode were determined through the modal analysis. The dispersion characteristics of TE and TM modes inside the waveguide were studied as they are important parameters determining how the optical pulse will evolve during the propagation through the waveguide. The zero dispersion wavelength for the fundamental TE mode of our designed waveguides was found to be near 1.55 μm.

Next, a thorough analysis of the spectral characteristics of the through and drop port intensity responses for single racetrack all-pass and add-drop ring resonators was presented. We have also studied how the gap between the ring and the straight waveguide affects the coupling. As the gap increases, less radiation gets coupled to the ring from the straight waveguide. However, during the fabrication process it was found that smaller gaps are very difficult to fabricate. Bearing in mind these facts,

we attempted to find a compromise value for the gap width, which was used in the design of our second sample.

The Q-factor describes the performance of a resonator. For the ring resonators the Q-factor is directly proportional to the length of the ring. But due to the accumulated propagation loss inside the ring, the Q-factor of a microring resonator exhibits a plateau after a certain round-trip length. Here, the highest Q-factor achievable is approximately 10400.

We have modeled the nonlinear four-wave mixing effect using our designed microring resonator and Lumerical MODE Solutions simulations. The simulations have shown that the new frequency component (the idler) gets generated when the frequencies of the signal and pump spectral components coincide with two resonances of the microring.

Finally, the fabrication process was described. Several attempts were made to fabricate the microring resonators devices. We describe the developed fabrication procedure and the conclusions that we draw from unsuccessful fabrication attempts. The experience we have gained is expected to help us to revisit the fabrication process in future attempts. The last fabrication attempt has resulted in a good quality sample with the microring resonators that is presently being tested for its optical performance.

In conclusion, we have designed microring resonators with high quality factor for enhanced four-wave mixing. The experimental work is under the way. Such devices have a potential to be used in optical communication networks for all-optical signal processing operations.

Bibliography

[1] Cisco, "Cisco visual networking index: Global mobile data traffic forecast update, 2015-2020 white paper." `http://www.cisco.com/c/en/us/solutions/collateral/service-provider/visual-networking-index-vni/white_paper_c11-520862.html`, 2016.

[2] T. Durhuus, B. Mikkelsen, C. Joergensen, S. L. Danielsen, and K. E. Stubkjaer, "All-optical wavelength conversion by semiconductor optical amplifiers," *Journal of Lightwave Technology*, vol. 14, no. 6, pp. 942–954, 1996.

[3] S. Nakamura, Y. Ueno, and K. Tajima, "168-gb/s all-optical wavelength conversion with a symmetric-mach-zehnder-type switch," *IEEE Photonics Technology Letters*, vol. 13, no. 10, pp. 1091–1093, 2001.

[4] R. G. Hunsperger and A. J. Maltenfort, "Optical wavelength division multiplexing/demultiplexing system," Sept. 20 1988. US Patent 4,773,063.

[5] D. Wolfson, A. Kloch, T. Fjelde, C. Janz, B. Dagens, and M. Renaud, "40-gb/s all-optical wavelength conversion, regeneration, and demultiplexing in an soa-based all-active mach-zehnder interferometer," *IEEE Photonics Technology Letters*, vol. 12, no. 3, pp. 332–334, 2000.

[6] A. Bogoni, X. Wu, I. Fazal, and A. E. Willner, "160 gb/s time-domain channel extraction/insertion and all-optical logic operations exploiting a single ppln

waveguide," *Journal of Lightwave Technology*, vol. 27, no. 19, pp. 4221–4227, 2009.

[7] R. Salem, M. A. Foster, A. C. Turner, D. F. Geraghty, M. Lipson, and A. L. Gaeta, "Signal regeneration using low-power four-wave mixing on silicon chip," *Nature Photonics*, vol. 2, no. 1, pp. 35–38, 2008.

[8] S. Madden, D.-Y. Choi, D. Bulla, A. V. Rode, B. Luther-Davies, V. G. Ta'eed, M. Pelusi, and B. J. Eggleton, "Long, low loss etched as 2 s 3 chalcogenide waveguides for all-optical signal regeneration," *Optics Express*, vol. 15, no. 22, pp. 14414–14421, 2007.

[9] M. Bajcsy, S. Hofferberth, V. Balic, T. Peyronel, M. Hafezi, A. S. Zibrov, V. Vuletic, and M. D. Lukin, "Efficient all-optical switching using slow light within a hollow fiber," *Physical Review Letters*, vol. 102, no. 20, p. 203902, 2009.

[10] E. Marcatili, "Bends in optical dielectric guides," *Bell System Technical Journal*, vol. 48, no. 7, pp. 2103–2132, 1969.

[11] L. F. Stokes, M. Chodorow, and H. J. Shaw, "All-single-mode fiber resonator," *Optics Letters*, vol. 7, no. 6, pp. 288–290, 1982.

[12] J. Haavisto and G. Pajer, "Resonance effects in low-loss ring waveguides," *Optics Letters*, vol. 5, no. 12, pp. 510–512, 1980.

[13] B. E. Little, S. T. Chu, H. A. Haus, J. Foresi, and J.-P. Laine, "Microring resonator channel dropping filters," *Journal of Lightwave Technology*, vol. 15, no. 6, pp. 998–1005, 1997.

[14] T. J. Kippenberg, R. Holzwarth, and S. Diddams, "Microresonator-based optical frequency combs," *Science*, vol. 332, no. 6029, pp. 555–559, 2011.

[15] H. Jung, C. Xiong, K. Y. Fong, X. Zhang, and H. X. Tang, "Optical frequency comb generation from aluminum nitride microring resonator," *Optics Letters*, vol. 38, no. 15, pp. 2810–2813, 2013.

[16] F. Ferdous, H. Miao, D. E. Leaird, K. Srinivasan, J. Wang, L. Chen, L. T. Varghese, and A. M. Weiner, "Spectral line-by-line pulse shaping of on-chip microresonator frequency combs," *Nature Photonics*, vol. 5, no. 12, pp. 770–776, 2011.

[17] T. Udem, R. Holzwarth, and T. W. Hänsch, "Optical frequency metrology," *Nature*, vol. 416, no. 6877, pp. 233–237, 2002.

[18] D. Hillerkuss, R. Schmogrow, T. Schellinger, M. Jordan, M. Winter, G. Huber, T. Vallaitis, R. Bonk, P. Kleinow, F. Frey, *et al.*, "26 tbit s-1 line-rate super-channel transmission utilizing all-optical fast fourier transform processing," *Nature Photonics*, vol. 5, no. 6, pp. 364–371, 2011.

[19] M. A. Popovic, T. Barwicz, M. S. Dahlem, F. Gan, C. W. Holzwarth, P. T. Rakich, H. I. Smith, E. P. Ippen, and F. X. Krtner, "Tunable fourth-order silicon microring-resonator add-drop filters," *ECOC 2007*, 2007.

[20] A. C. Turner, M. A. Foster, A. L. Gaeta, and M. Lipson, "Ultra-low power parametric frequency conversion in a silicon microring resonator," *Optics Express*, vol. 16, no. 7, pp. 4881–4887, 2008.

[21] S. Xiao, L. Liu, and M. Qiu, "Resonator channel drop filters in a plasmon-polaritons metal," *Optics Express*, vol. 14, no. 7, pp. 2932–2937, 2006.

[22] P. Dong, W. Qian, H. Liang, R. Shafiiha, N.-N. Feng, D. Feng, X. Zheng, A. V. Krishnamoorthy, and M. Asghari, "Low power and compact reconfigurable mul-

tiplexing devices based on silicon microring resonators," *Optics Express*, vol. 18, no. 10, pp. 9852–9858, 2010.

[23] P. Dong, W. Qian, H. Liang, R. Shafiiha, X. Wang, D. Feng, G. Li, J. E. Cunningham, A. V. Krishnamoorthy, and M. Asghari, "1x4 reconfigurable demultiplexing filter based on free-standing silicon racetrack resonators," *Optics Express*, vol. 18, no. 24, pp. 24504–24509, 2010.

[24] C.-Y. Chao, W. Fung, and L. J. Guo, "Polymer microring resonators for biochemical sensing applications," *IEEE Journal of Selected Topics in Quantum Electronics*, vol. 12, no. 1, pp. 134–142, 2006.

[25] K. De Vos, I. Bartolozzi, E. Schacht, P. Bienstman, and R. Baets, "Silicon-on-insulator microring resonator for sensitive and label-free biosensing," *Optics Express*, vol. 15, no. 12, pp. 7610–7615, 2007.

[26] A. Yalcin, K. C. Popat, J. C. Aldridge, T. A. Desai, J. Hryniewicz, N. Chbouki, B. E. Little, O. King, V. Van, S. Chu, *et al.*, "Optical sensing of biomolecules using microring resonators," *IEEE Journal of Selected Topics in Quantum Electronics*, vol. 12, no. 1, pp. 148–155, 2006.

[27] S.-W. Huang, S.-L. Chen, T. Ling, A. Maxwell, M. ODonnell, L. J. Guo, and S. Ashkenazi, "Low-noise wideband ultrasound detection using polymer microring resonators," *Applied Physics Letters*, vol. 92, no. 19, p. 193509, 2008.

[28] B. Bhola, P. Nosovitskiy, H. Mahalingam, and W. H. Steier, "Sol-gel-based integrated optical microring resonator humidity sensor," *IEEE Sensors Journal*, vol. 9, no. 7, pp. 740–747, 2009.

[29] P. Sanati, A. Afroozeh, I. Amiri, J. Ali, and L. S. Chua, "Femtosecond pulse generation using microring resonators for eye nano surgery," *Nanoscience and Nanotechnology Letters*, vol. 6, no. 3, pp. 221–226, 2014.

[30] H. Tsang and Y. Liu, "Nonlinear optical properties of silicon waveguides," *Semiconductor Science and Technology*, vol. 23, no. 6, p. 064007, 2008.

[31] M. A. Foster, A. C. Turner, M. Lipson, and A. L. Gaeta, "Nonlinear optics in photonic nanowires," *Optics Express*, vol. 16, no. 2, pp. 1300–1320, 2008.

[32] E. Dulkeith, Y. A. Vlasov, X. Chen, N. C. Panoiu, and R. M. Osgood, "Self-phase-modulation in submicron silicon-on-insulator photonic wires," *Optics Express*, vol. 14, no. 12, pp. 5524–5534, 2006.

[33] T. Liang and H. Tsang, "Role of free carriers from two-photon absorption in raman amplification in silicon-on-insulator waveguides," *Applied Physics Letters*, vol. 84, no. 15, pp. 2745–2747, 2004.

[34] D. Chemla, D. Miller, P. Smith, A. Gossard, and W. Wiegmann, "Room temperature excitonic nonlinear absorption and refraction in gaas/algaas multiple quantum well structures," *IEEE Journal of Quantum Electronics*, vol. 20, no. 3, pp. 265–275, 1984.

[35] S. Gehrsitz, F. Reinhart, C. Gourgon, N. Herres, A. Vonlanthen, and H. Sigg, "The refractive index of alxga1- xas below the band gap: Accurate determination and empirical modeling," *Journal of Applied Physics*, vol. 87, no. 11, pp. 7825–7837, 2000.

[36] E. H. Li, "Material parameters of ingaasp and inalgaas systems for use in quantum well structures at low and room temperatures," *Physica E: Low-dimensional systems and Nanostructures*, vol. 5, no. 4, pp. 215–273, 2000.

[37] H. Tanaka, Y. Kawamura, S. Nojima, K. Wakita, and H. Asahi, "Ingap/ingaalp double-heterostructure and multiquantum-well laser diodes grown by molecular-beam epitaxy," *Journal of Applied Physics*, vol. 61, no. 5, pp. 1713–1719, 1987.

[38] M. Tchernycheva, G. E. Cirlin, G. Patriarche, L. Travers, V. Zwiller, U. Perinetti, and J.-C. Harmand, "Growth and characterization of inp nanowires with inasp insertions," *Nano Letters*, vol. 7, no. 6, pp. 1500–1504, 2007.

[39] M. Yamamoto, N. Yamamoto, and J. Nakano, "Movpe growth of strained inasp/ingaasp quantum-well structures for low-threshold 1.3-μm lasers," *IEEE Journal of Quantum Electronics*, vol. 30, no. 2, pp. 554–561, 1994.

[40] D. F. Feezell, J. S. Speck, S. P. DenBaars, and S. Nakamura, "Semipolar ingan/gan light-emitting diodes for high-efficiency solid-state lighting," *Journal of Display Technology*, vol. 9, no. 4, pp. 190–198, 2013.

[41] R. Goldhahn, J. Scheiner, S. Shokhovets, T. Frey, U. Köhler, D. As, and K. Lischka, "Refractive index and gap energy of cubic inxga1- xn," *Applied Physics Letters*, vol. 76, no. 3, pp. 291–293, 2000.

[42] S. Nakamura, S. Pearton, and G. Fasol, *The blue laser diode: the complete story*. Springer Science & Business Media, 2013.

[43] V. Shamakhov, D. Nikolaev, A. Lyutetskiy, K. Bakhvalov, M. Rastegaeva, S. Slipchenko, N. Pikhtin, and I. Tarasov, "Laser-diode bars based on algaasp/gaas heterostructures emitting at a wavelength of 850 nm," *Semiconductors*, vol. 48, no. 3, pp. 373–376, 2014.

[44] G. Stegeman, A. Villeneuve, J. Kang, J. Aitchison, C. Ironside, K. Al-Hemyari, C. Yang, C.-H. Lin, H.-H. Lin, G. Kennedy, *et al.*, "Algaas below half bandgap:

the silicon of nonlinear optical materials," *International Journal of Nonlinear Optical Physics*, vol. 3, no. 03, pp. 347–371, 1994.

[45] A. Villeneuve, J. Aitchison, B. Vögele, R. Tapella, J. Kang, C. Trevino, and G. Stegeman, "Waveguide design for minimum nonlinear effective area and switching energy in algaas at half the bandgap," *Electronics Letters*, vol. 31, no. 7, pp. 549–551, 1995.

[46] J. Aitchison, D. Hutchings, J. Kang, G. Stegeman, and A. Villeneuve, "The nonlinear optical properties of algaas at the half band gap," *IEEE Journal of Quantum Electronics*, vol. 33, no. 3, pp. 341–348, 1997.

[47] G. A. Siviloglou, S. Suntsov, R. El-Ganainy, R. Iwanow, G. I. Stegeman, D. N. Christodoulides, R. Morandotti, D. Modotto, A. Locatelli, C. De Angelis, *et al.*, "Enhanced third-order nonlinear effects in optical algaas nanowires," *Optics Express*, vol. 14, no. 20, pp. 9377–9384, 2006.

[48] K. Dolgaleva, W. C. Ng, L. Qian, and J. S. Aitchison, "Compact highly-nonlinear algaas waveguides for efficient wavelength conversion," *Optics Express*, vol. 19, no. 13, pp. 12440–12455, 2011.

[49] M. M. Choy and R. L. Byer, "Accurate second-order susceptibility measurements of visible and infrared nonlinear crystals," *Physical Review B*, vol. 14, no. 4, p. 1693, 1976.

[50] P. Apiratikul, J. J. Wathen, G. A. Porkolab, B. Wang, L. He, T. E. Murphy, and C. J. Richardson, "Enhanced continuous-wave four-wave mixing efficiency in nonlinear algaas waveguides," *Optics Express*, vol. 22, no. 22, pp. 26814–26824, 2014.

[51] A. Yariv, "Universal relations for coupling of optical power between microresonators and dielectric waveguides," *Electronics Letters*, vol. 36, no. 4, pp. 321–322, 2000.

[52] J. M. Choi, R. K. Lee, and A. Yariv, "Control of critical coupling in a ring resonator–fiber configuration: application to wavelength-selective switching, modulation, amplification, and oscillation," *Optics Letters*, vol. 26, no. 16, pp. 1236–1238, 2001.

[53] V. M. Menon, W. Tong, and S. R. Forrest, "Manipulation of cavity q and critical coupling in a microring resonator through integration of a semiconductor optical amplifier," in *Conference on Lasers and Electro-Optics*, p. CTuFF6, Optical Society of America, 2004.

[54] J. Heebner, R. Grover, T. Ibrahim, and T. A. Ibrahim, *Optical microresonators: theory, fabrication, and applications*. Springer Science & Business Media, 2008.

[55] W. Bogaerts, P. De Heyn, T. Van Vaerenbergh, K. De Vos, S. Kumar Selvaraja, T. Claes, P. Dumon, P. Bienstman, D. Van Thourhout, and R. Baets, "Silicon microring resonators," *Laser & Photonics Reviews*, vol. 6, no. 1, pp. 47–73, 2012.

[56] J. E. Heebner and R. W. , "Enhanced all-optical switching by use of a nonlinear fiber ring resonator," *Optics Letters*, vol. 24, no. 12, pp. 847–849, 1999.

[57] P. Absil, J. Hryniewicz, B. Little, R. Wilson, L. Joneckis, and P.-T. Ho, "Compact microring notch filters," *Photonics Technology Letters, IEEE*, vol. 12, no. 4, pp. 398–400, 2000.

[58] C. Manolatou, M. Khan, S. Fan, P. R. Villeneuve, H. Haus, and J. Joannopoulos, "Coupling of modes analysis of resonant channel add-drop filters," *IEEE Journal of Quantum Electronics*, vol. 35, no. 9, pp. 1322–1331, 1999.

[59] Y. Zhang, X. Liu, X. Zhang, and P. Yuan, "Coupled add-drop ring resonator for highly sensitive sensing," in *Sensing Technology (ICST), 2013 Seventh International Conference on*, pp. 365–368, IEEE, 2013.

[60] H. Yan, X. Feng, D. Zhang, K. Cui, F. Liu, and Y. Huang, "Compact optical add-drop multiplexers with parent-sub ring resonators on soi substrates," *Photonics Technology Letters, IEEE*, vol. 25, no. 15, pp. 1462–1465, 2013.

[61] W. Zhang, W. Liu, W. Li, H. Shahoei, and J. Yao, "Independently tunable multichannel fractional-order temporal differentiator based on a silicon-photonic symmetric mach–zehnder interferometer incorporating cascaded microring resonators," *Journal of Lightwave Technology*, vol. 33, no. 2, pp. 361–367, 2015.

[62] J. Dong, A. Zheng, D. Gao, S. Liao, L. Lei, D. Huang, and X. Zhang, "High-order photonic differentiator employing on-chip cascaded microring resonators," *Optics Letters*, vol. 38, no. 5, pp. 628–630, 2013.

[63] Y. Hu, X. Xiao, H. Xu, X. Li, K. Xiong, Z. Li, T. Chu, Y. Yu, and J. Yu, "High-speed silicon modulator based on cascaded microring resonators," *Optics Express*, vol. 20, no. 14, pp. 15079–15085, 2012.

[64] L. Yang, C. Guo, W. Zhu, L. Zhang, and C. Sun, "Demonstration of a directed optical comparator based on two cascaded microring resonators," *IEEE Photonics Technology Letters*, vol. 27, no. 8, pp. 809–812, 2015.

[65] M. Mao, S. Chen, and D. Dai, "Cascaded ring-resonators for multi-channel optical sensing with reduced temperature sensitivity," *IEEE Photonics Technology Letters*, vol. 28, no. 7, pp. 814–817, 2016.

[66] D. G. Rabus, *Integrated ring resonators*. Springer, 2007.

[67] R. W. Boyd, *Nonlinear optics*. Academic Press, 2003.

[68] C. Langrock, S. Kumar, J. E. McGeehan, A. Willner, and M. Fejer, "All-optical signal processing using χ (2) nonlinearities in guided-wave devices," *Journal of Lightwave Technology*, vol. 24, no. 7, pp. 2579–2592, 2006.

[69] G. P. Agrawal, *Nonlinear Fiber Optics*. Academic Press, 2007.

[70] L. Yan, A. E. Willner, X. Wu, A. Yi, A. Bogoni, Z.-Y. Chen, and H.-Y. Jiang, "All-optical signal processing for ultrahigh speed optical systems and networks," *Journal of Lightwave Technology*, vol. 30, no. 24, pp. 3760–3770, 2012.

[71] S. Kawanishi and O. Kamatani, "All-optical time division multiplexing using four-wave mixing," *Electronics Letters*, vol. 30, no. 20, pp. 1697–1698, 1994.

[72] P. A. Andrekson, N. Olsson, J. Simpson, T. Tanbun-Ek, R. Logan, and M. Haner, "16 gbit/s all-optical demultiplexing using four-wave mixing," *Electronics Letters*, vol. 27, no. 11, pp. 922–924, 1991.

[73] R. Stolen and C. Lin, "Self-phase-modulation in silica optical fibers," *Physical Review A*, vol. 17, no. 4, p. 1448, 1978.

[74] G. P. Agrawal and N. A. Olsson, "Self-phase modulation and spectral broadening of optical pulses in semiconductor laser amplifiers," *IEEE Journal of Quantum Electronics*, vol. 25, no. 11, pp. 2297–2306, 1989.

[75] O. Boyraz, T. Indukuri, and B. Jalali, "Self-phase-modulation induced spectral broadening in silicon waveguides," *Optics Express*, vol. 12, no. 5, pp. 829–834, 2004.

[76] Y. Shen and G.-Z. Yang, "Theory of self-phase modulation and spectral broadening," in *The Supercontinuum Laser Source*, pp. 1–32, Springer, 1989.

[77] Z. Zang and Y. Zhang, "Analysis of optical switching in a yb 3+-doped fiber bragg grating by using self-phase modulation and cross-phase modulation," *Applied Optics*, vol. 51, no. 16, pp. 3424–3430, 2012.

[78] J. K. Ranka, R. S. Windeler, and A. J. Stentz, "Visible continuum generation in air-silica microstructure optical fibers with anomalous dispersion at 800 nm," *Optics Letters*, vol. 25, no. 1, pp. 25–27, 2000.

[79] S. Akhmanov, R. Khokhlov, and A. Sukhorukov, "Self-focusing, self-defocusing and self-modulation of laser beams," *Laser Handbook*, vol. 2, pp. 1151–1228, 1972.

[80] M. Galili, L. K. Oxenløwe, H. C. H. Mulvad, A. Clausen, and P. Jeppesen, "Optical wavelength conversion by cross-phase modulation of data signals up to 640 gb/s," *IEEE Journal on Selected Topics in Quantum Electronics*, vol. 14, no. 3, pp. 573–579, 2008.

[81] H. Tsuchida, T. Simoyama, H. Ishikawa, T. Mozume, M. Nagase, and J.-i. Kasai, "Cross-phase-modulation-based wavelength conversion using intersubband transition in ingaas/alas/alassb coupled quantum wells," *Optics Letters*, vol. 32, no. 7, pp. 751–753, 2007.

[82] M. Jazayerifar, L. Zhou, L. Zimmermann, K. Pertermann, *et al.*, "Cross-phase modulation (xpm)-induced all optical switching in a coupling-tuned silicon ring resonator," in *Asia Communications and Photonics Conference*, pp. AS4J–3, Optical Society of America, 2015.

[83] J. S. Pelc, K. Rivoire, S. Vo, C. Santori, D. A. Fattal, and R. G. Beausoleil, "Picosecond all-optical switching in hydrogenated amorphous silicon microring resonators," *Optics Express*, vol. 22, no. 4, pp. 3797–3810, 2014.

[84] A. M. Weiner, Y. Silberberg, H. Fouckhardt, D. E. Leaird, M. Saifi, M. Andrejco, and P. W. Smith, "Use of femtosecond square pulses to avoid pulse breakup in all-optical switching," *IEEE Journal of Quantum Electronics*, vol. 25, no. 12, pp. 2648–2655, 1989.

[85] B. J. Eggleton, T. D. Vo, R. Pant, J. Schr, M. D. Pelusi, D. Yong Choi, S. J. Madden, and B. Luther-Davies, "Photonic chip based ultrafast optical processing based on high nonlinearity dispersion engineered chalcogenide waveguides," *Laser & Photonics Reviews*, vol. 6, no. 1, pp. 97–114, 2012.

[86] K. P. Jackson, S. A. Newton, B. Moslehi, M. Tur, C. C. Cutler, J. W. Goodman, and H. Shaw, "Optical fiber delay-line signal processing," *IEEE Transactions on Microwave Theory and Techniques*, vol. 33, no. 3, pp. 193–210, 1985.

[87] J. Cardenas, M. A. Foster, N. Sherwood-Droz, C. B. Poitras, H. L. Lira, B. Zhang, A. L. Gaeta, J. B. Khurgin, P. Morton, and M. Lipson, "Wide-bandwidth continuously tunable optical delay line using silicon microring resonators," *Optics Express*, vol. 18, no. 25, pp. 26525–26534, 2010.

[88] Z. Yu, Q. Zhang, H. Wang, J. Zhang, and D. R. Selviah, "Tunable optical delay line for optical time-division multiplexer," *Optics Communications*, 2016.

[89] N. P. Group, "Optical time division multiplexing." `http://www.http://nonlinearphotonics.ca`, 2015.

[90] L. M. Solution, "Finite difference eigenmode (fde) solver." `https://kb.lumerical.com/en/index.html?solvers_finite_difference_eigenmode.html`.

[91] J. Meier, W. Mohammed, A. Jugessur, L. Qian, M. Mojahedi, and J. Aitchison, "Group velocity inversion in algaas nanowires," *Optics Express*, vol. 15, no. 20, pp. 12755–12762, 2007.

[92] K. Dolgaleva, P. Sarrafi, P. Kultavewuti, K. M. Awan, N. Feher, J. S. Aitchison, L. Qian, M. Volatier, R. Arès, and V. Aimez, "Tuneable four-wave mixing in algaas nanowires," *Optics Express*, vol. 23, no. 17, pp. 22477–22493, 2015.

[93] J. Pan and Y. Shi, "Dense wdm multiplexer and demultiplexer with 0.4 nm channel spacing," *Electronics Letters*, vol. 34, no. 1, pp. 74–75, 1998.

[94] Q. Xu, B. Schmidt, J. Shakya, and M. Lipson, "Cascaded silicon micro-ring modulators for wdm optical interconnection," *Optics Express*, vol. 14, no. 20, pp. 9431–9436, 2006.

[95] Y. Sugimoto, N. Ikeda, N. Carlsson, K. Asakawa, N. Kawai, and K. Inoue, "Fabrication and characterization of different types of two-dimensional algaas photonic crystal slabs," *Journal of Applied Physics*, vol. 91, no. 3, pp. 922–929, 2002.

[96] R. Boyd, J. Heebner, N. Lepeshkin, Q.-H. Park, A. Schweinsberg, G. Wicks, A. Baca, J. Fajardo, R. Hancock, M. Lewis, *et al.*, "Nanofabrication of optical structures and devices for photonics and biophotonics," *Journal of Modern Optics*, vol. 50, no. 15-17, pp. 2543–2550, 2003.

[97] A. Grigorescu, M. Van der Krogt, C. Hagen, and P. Kruit, "10nm lines and spaces written in hsq, using electron beam lithography," *Microelectronic Engineering*, vol. 84, no. 5, pp. 822–824, 2007.

[98] P. Kultavewuti, V. Pusino, M. Sorel, and J. S. Aitchison, "Low-power continuous-wave four-wave mixing wavelength conversion in algaas-nanowaveguide microresonators," *Optics Letters*, vol. 40, no. 13, pp. 3029–3032, 2015.